COMMISSION ON POWDER DIFFRACTION

INTERNATIONAL UNION OF CRYSTALLOGRAPHY
http://www.iucr-cpd.org/

NEWSLETTER No. 34, December 2007
http://www.iucr-cpd.org/Newsletters.htm

IN THIS ISSUE

Microstructure Analysis on Nanocrystalline Materials

(David Rafaja, Editor)

ISSN 1591-9552

CPD Chairman's Message

Powder diffraction is traditionally seen as a technique for the determination and refinement of moderately complex crystal structures that are difficult to prepare as single crystals for X-ray diffraction analysis. Many people see powder diffraction and the Rietveld technique as synonymous with one another. However, there is an important class of materials where micron-sized single crystals are simply not available – nanomaterials and nanocomposites. This current newsletter focuses on the developments and successes in using X-ray powder diffraction to analyse nanocrystalline systems. High resolution and high statistical accuracy mean that precise, detailed structural and microstructural studies of nanomaterials may be performed using powder diffraction. These reciprocal space studies complement and augment transmission electron microscopy measurements and show that powder diffraction has a relevance to the real world that ranges from nanometre to millimetre lengthscales.

Bill David

From the Editor of Newsletter 34

For microstructure analysis on nanocrystalline materials and nanocomposites, transmission electron microscopy is the technique of choice. However, in this issue of the Commission on Powder Diffraction Newsletter, we show that recent developments in instrumentation and analysis mean that X-ray powder diffraction still has a huge potential. Indeed, it is only the combination of these experimental methods, supplemented by other techniques such as spectroscopy that yields a complete understanding of the microstructure of nanomaterials.

Traditional advantages of the powder X-ray diffraction are its high statistical relevance and the non-destructive nature of the sample preparation, which still favour the powder X-ray diffraction in comparison with the transmission electron microscopy. Other advantages of the powder X-ray diffraction are the excellent resolution in reciprocal space and high sensitivity to the crystal anisotropy of the interplanar spacing and its changes that are much better than for TEM.

The papers in this issue present diffraction phenomena and experimental results obtained over several orders of magnitude: from clusters of atoms (individual nanocrystallites) and of partially coherent nanocrystallites, through nanocrystallites containing structure defects to sub-microcrystalline materials obtained by severe plastic deformation and precipitates with mutual distances in sub-micrometer range.

David Rafaja

WWW sites related to powder diffraction

The Commission on Powder Diffraction (CPD):	http://www.iucr-cpd.org/
The International Union of Crystallography (IUCr):	http://www.iucr.org/
The International Centre for Diffraction Data (ICDD):	http://www.icdd.com/
The International X-ray Analysis Society (IXAS):	http://www.ixas.org/
Collaborative Computational Project #14 (CCP 14):	http://www.ccp14.ac.uk/

Submitting a proposal for neutron diffraction or synchrotron radiation X-ray diffraction is possible at many (publicly funded) large scale facilities in the world. It represents an important and frequently unique opportunity for powder diffraction experiments. A useful guide and information can be accessed through the following web-site, maintained by R. Dinnebier at http://www.pulverdiffraktometrie.de/. This list is far from being complete and needs input from users and readers of the CPD Newsletter. Please send comments to *R. Dinnebier* (r.dinnebier@fkf.mpg.de)

CPD project

Rietveld refinement of organic structures

Increasing numbers of organic crystal structures are being solved and refined from powder diffraction data. The basic arrangement of the molecules in the structure can often be determined by direct methods, or by direct-space approaches. However, experience shows that problems can arise in the subsequent Rietveld refinement. For example, unless restrained by appropriate bond distances and angles molecules can distort unrealistically from a reasonable molecular structure. So how good are these Rietveld refinements? Is the problem a fundamental one of powder diffraction? e.g. the ambiguities and correlations caused by peak overlap or defining the background etc. lead to inaccurate structures. Or can some of the blame be attributed to poor refinement practice? We plan to put onto the CPD web site a number of good quality powder diffraction patterns from organic compounds of known crystal structure and of different complexity. These can be downloaded, and powder crystallographers can try out their own prowess at Rietveld refinement, by comparing their refined structures with the accepted single-crystal structures. This should be a learning exercise for us all. Any suggestions as to compounds that would appear particularly appropriate for this project are very welcome. Please contact the CPD chairman, Bill David, at bill.david@rl.ac.uk.

The IUCr Commission on Powder Diffraction - Triennium 2005-2008

Chairman: Prof. W. I. F. David (Bill)
Rutherford Appleton Laboratory (CCLRC), Chilton, Oxon
OX11 OQX, United Kingdom
Telephone: +44 1235 445179 | Fax: +44 1235 445642
e-mail: W.I.F.David@rl.ac.uk

Secretary: Prof. A. N. Fitch (Andy)
ESRF, BP220, F-38043 Grenoble Cedex 9, France
Telephone : +33 476 88 25 32 | Fax: +33 476 88 25 42
e-mail: fitch@esrf.fr

Prof. S.J.L. Billinge (Simon)
Department of Physics and Astronomy,
Michigan State University, East Lansing, MI 48824,
U.S.A.
Telephone: +1 517 353 8697 | Fax: +1 517 353 4500
e-mail: billinge@pa.msu.edu

Prof. M. Delgado (Miguel)
Laboratorio de Cristalografía, Departamento de Química,
Facultad de Ciencias, Universidad de Los Andes, P.O. Box
40, La Hechicera, Mérida 5251, Venezuela
Telephone: +58 274 240 1372 | Fax: +58 274 240 1286
e-mail: migueld@ula.ve

Dr. I. Madsen (Ian)
CSIRO Minerals
Box 312, Clayton South 3169, Victoria, Australia
Telephone: +61 3 9545 8785 | Fax: +61 3 9562 8919
e-mail: Ian.Madsen@csiro.au

Prof. N. Masciocchi (Norberto)
Dipartimento di Scienze Chimiche e Ambientali,
Università dell' Insubria, via Valleggio 11, I-22100 Como,
Italy
Telephone: +39 031 326227 | Fax: +39-031-2386119
e-mail: norberto.masciocchi@uninsubria.it

Prof. D. Rafaja (David)
Institut für Werkstoffwissenschaft, TU Bergakademie Freiberg,
Gustav-Zeuner-Str. 5, D-09599 Freiberg,
Germany
Telephone: +49 3731 39 2299 | Fax: +49 3731 39 3657
e-mail: Rafaja@ww.tu-freiberg.de

Dr. R. Rizzi (Rosanna)
CNR IC – c/o Dip. Geomineralogico, Via Orabona 4,
I-70125 Bari, Italy
Telephone: + 39 80 544 2624 | Fax: + 39 80 544 2591
e-mail: rosanna.rizzi@ic.cnr.it

Prof. P. Stephens (Peter)
Department of Physics and Astronomy
Stony Brook University, Stony Brook, NY 11794-3800,
USA
Telephone: +1 631 632 8156 | Fax: +1 631 632 4977
e-mail: pstephens@notes.cc.sunysb.edu

Dr. P. Whitfield (Pam)
Institute for Chemical Process and Environmental Technology,
National Research Council Canada, Building M12, 1200
Montreal Road, Ottawa, Ontario, K1A 0R6, Canada
Telephone: +1 613 998 8462 | Fax: +1 613 991 2384
e-mail: Pamela.Whitfield@cnrc-nrc.gc.ca

Consultants

Dr. J. Cline (Jim)
Ceramics Division (852), NIST, 100 Bureau Drive,
Stop 8520, Gaithersburg, MD 20899, USA
Telephone: +1 301 975 5793
e-mail: james.cline@nist.gov

Dr. R. E. Dinnebier (Robert)
Max-Planck-Institut für Festkörperforschung,
Heisenbergstrasse 1, D-70569 Stuttgart, Germany
Telephone: +49 711 689 1503 | Fax: +49 711 689 1502
e-mail: r.dinnebier@fkf.mpg.de

Prof. P. Scardi (Paolo)
Dipartimento di Ingegneria dei Materiali e Tecnologie
Industriali, Università di Trento, I-38050 Mesiano (TN), Italy
Telephone: +39 0461 882417/67 | Fax: +39 0461 881977
e-mail: Paolo.Scardi@ing.unitn.it

Prof. J. De Villiers (Johan)
Mineral Division MINTEK, Private Bag X3015, Randburg
2125, South Africa
Telephone: +27 11 709 4745 | Fax: +27 11 709 4564
e-mail: jpdev@postino.up.ac.za

Dr. I. Margiolaki (Irene)
ESRF, BP 220, F-38043 Grenoble Cedex, France
Telephone: +33 476 88 2148 | Fax: +33 476 88 2907
e-mail: margiolaki@esrf.fr

Prof. M. Yashima (Masatomo)
Tokyo Institute of Technology, Grad. School of Science and
Engineering, Department of Materials Science and Engineering,
Nagatsuta-cho 4259-J1-4,
Midori-ku Yokohama, 226-8502, Japan
Telephone: +81-45-924-5630 | Fax: +81-45-924-5630
e-mail: yashima@materia.titech.ac.jp

ICDD Representative
Dr. J. Kaduk (Jim)
INEOS Technologies, Analytical Science Research Services,
MC F-9, P.O. Box 3011, 150 W. Warrenville Road,
Naperville IL 60566-7011
Telephone: +1 630 420 4547 | Fax: +1 630 420 5252
e-mail: james.kaduk@innovene.com

A WHOLE POWDER PATTERN METHOD FOR NANOPARTICLE CHARACTERIZATION

Antonio Cervellino[1,], Cinzia Giannini[2], Antonietta Guagliardi[2]*

1. Laboratory for Neutron Scattering, ETH Zurich and PSI Villigen, CH-5232 Villigen PSI, Switzerland

2. Istituto di Cristallografia, CNR
Via Amendola 122/O, 70126 Bari, ITALY

e-mail: cinzia.giannini@ic.cnr.it

INTRODUCTION

The quantitative analysis of powder diffraction patterns collected on nanocrystals constitutes a complex problem of data analysis. Significant differences distinguish a nanomaterial from a micrometric one, as summarized in Fig. 1. A contribution to the pattern of utmost importance comes from the size (and the size distribution), especially for very small particles (1-2 nm), where the diffraction peak width can reach several degrees. Another important contribution derives from the surface. At extremely small sizes the ratio of surface to volume atoms may easily exceed 50% (see Fig. 1). Surface atom positions differ from the bulk because of reconstruction, and, in addition, due to the surface strain fields that normally occur due to surfactants. This surface effect is size dependent. Therefore, at least a size dependent unit cell should be modelled to account for the surface effect [1]. In some specific cases, such as for noble metals, a nanocrystalline sample is realistically composed by more structures; some of them even non crystallographic (icosahedra, decahedra). The latter cannot be described as a portion of a periodic lattice and have a five-fold symmetry axis. This further level of complexity rules out any traditional crystallographic method.

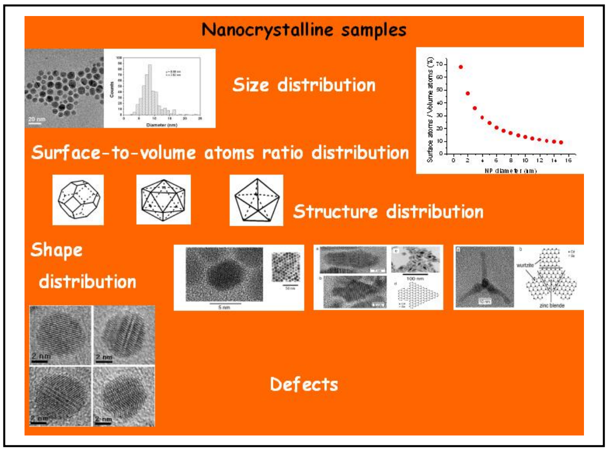

Fig. 1. *Schematic illustration of the most important features of nanocrystalline sample.*

Finally, a complete method should be able to treat nanoparticles of whatever shape (sphere, rod, tetrapod etc) as needed for many technological compounds recently synthesized. Especially for larger nanoparticles, defects (stacking faults, anti-phase domains etc) are also expected and should be added into the model.

These are the most important aspects to consider for making a method of quantitative microstructural analysis successful for nanocrystals. Our choice has been to use the Debye function (DF) for the diffracted intensity calculation. This choice was firstly motivated by the need to treat diffraction data collected on noble metals, as the Debye function does not require lattice periodicity. Additional advantages of the DF pattern calculation with respect to the shape-based convolution approach [7] convinced us to select this method as the most appropriate approach for structural analysis on nanocrystals. In the following, we will briefly describe the method and give some applications.

FROM THE CLUSTER TO THE PATTERN

Few basic steps have to be fulfilled to calculate the diffraction pattern:

1. *Constructing the atomic models for clusters of increasing size up to a maximum diameter provided by the user.* In the case of spherical shape, clusters are made of concentric shells added in discrete numbers (onion-like model). The size step corresponds to a spherical shell whose volume contains an entire number of formula units.
2. C*alculating the corresponding interatomic distances database*. Our approach has been to generate few databases corresponding to some relevant crystallographic prototypes (diamond, rocksalt, fcc, rutile, zincblende and wurtzite [2]) as well as to generate the databases for some non crystallographic structures (icosahedra, decahedra and truncated decahedra). Any nanocrystal having one of the listed prototypes, or alternatively, any mono-atomic noble metal (Au, Ag) which is known to crystallize in fcc but also according to other non crystallographic structures, can be treated within this approach. It is necessary to select the correct database, re-scale the interatomic distances using the proper unit cell and substitute the proper atomic species.
3. F*or each structure in the sample a log-normal size distribution and size dependent strain distribution have to be provided*. In the case of nanocrystals of spherical shape, a uniform and isotropic surface-led radial deformation inside each single nanoparticle was chosen as strain function.

The shortcoming of this approach is the huge number of distances to be considered, even grouping the equal ones, with grim perspective with respect to the calculation times and the possibility of applying iterative optimisation algorithms like non linear least-squares. Therefore, a distances sampling algorithm, inspired to Ten Eyck's idea [3], is applied to each database: each distance is convoluted in direct space with a Gaussian function, summing up all these Gaussian functions to obtain a continuous atomic pair distance distribution (PDF), which is then sampled on a fixed grid with a suitable step δ ($\delta < \Delta$, the width of Gaussians). The number of interatomic distances is drastically reduced by sampling, as shown in Table I, choosing Au nanocrystals in the icosahedral structure.

Once the sampled interatomic distance database is available and the size and strain distribution functions are chosen, the pattern intensity can be easily computed using a fast algorithm performing the Debye Function, thanks to the constant step of the sampled distances [4]. The details of the pattern intensity calculation and interatomic distances sampling are given in [4, 5]. A brief description of the software NANO which presently implements our method is described in [6]. With respect to the version described in [6] the refinement section has been modified alternating COMPLEX, Simulating Annealing and Full-Newton Least Squares algorithms.

n	*d(nm)*	*Atoms*	*Interatomic distances*	*Gaussian sampled distances*
5	2.143	561	$1.6 \cdot 10^5$	362
10	4.524	3871	$7.5 \cdot 10^6$	705
20	9.286	28741	$4.0 \cdot 10^8$	1412
50	23.573	429351	$9.0 \cdot 10^{10}$	3534

Table I. *n* = cluster shell number, *d* = cluster diameter, interatomic distances and Gaussian sampled distances valid up to $q_{max} = \frac{2\sin\theta_{max}}{\lambda} = 1.25 Å^{-1}$.

APPLICATIONS

PbS nanoparticles

Colloidals PbS nanoparticles in the size range 4-7 nm have been studied by HRTEM and XRPD to determine the particle size in order to calculate the extinction coefficients [7]. One of the samples involved in this work was analyzed with this approach (an extensive application was not possible because the samples are all affected by texture effects, not yet available in the model). We generated spherical PbS clusters up to about 20 nm in diameter (prototype rocksalt, Pearson symbol cF8). The structural information was taken by ICSD #38293, with a cell parameter a=5.934 Å.

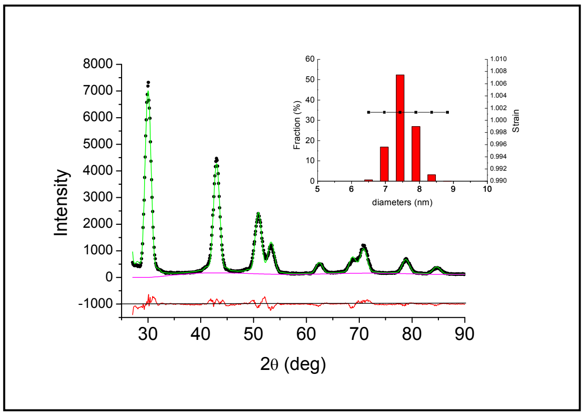

Fig. 2. *PbS XRPD experimental dataset and relevant calculated pattern. Background and difference profiles are included. Size & Strain distribution are shown in the inset. GoF=2.54, Rwp=10.32.*

Refined parameters were: the centre and width of the lognormal size distribution, strain parameters and the background coefficients. The final best fit is shown in Fig. 2 together with the size and strain distributions (in the inset).

The tensile strain of about 0.001, independent of the size, can be also interpreted as a larger unit cell (a = 5.942 Å) in agreement with the refined value that was found when the data were modelled using a shape-based convolution approach described in [8].

Iron oxide nanoparticles

Maghemite nanoparticles have been synthesized with an original chemical route obtaining nanocrystals of different shapes according to the reaction parameters [9]. In Fig. 3 the diffraction patterns collected on spherical shape nanocrystals (solid line) and on tetrapods (dotted curve) are shown. The shape clearly affects the width and intensity ratio. A gradual increase in the I_{220}/I_{511} and especially in the I_{440}/I_{311} ratio accompanies the transition from the spherical to the tetrapod shape with progressively longer branches. It is also noted that the (111) and (220) peak maxima slightly shift to higher angles. We first started data analysis with the sample having a spherical shape.

Within our approach we generated spherical maghemite clusters up to about 10 nm in diameter. The structural information[1] was taken by ICSD #87119 (Pearson symbol cP53), with a cell parameter a = 8.3457 Å. Refined parameters were: centre and width of the lognormal size distribution, the isotropic thermal parameters and the background coefficients. The final best fit is shown in Fig. 4 together with the size and strain distributions (in the inset).

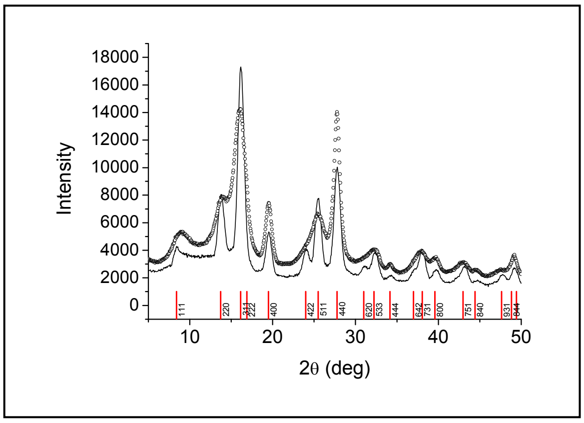

Fig. 3. *Iron Oxide XRPD experimental datasets: the solid and dotted lines correspond to spherical and tetrapod shape nanocrystals, respectively.*

The atomic models for tetrapods (TPs) with arms oriented along the [110], [111] and [100] orientations were generated and the corresponding diffraction patterns were calculated. Dotted and solid curves are computed for TPs with different arm length (l) and di-

---

[1] It is worth noting that for this structure, cluster's generation takes into account the partial occupancy of some atoms.

ameter (d): l = 20Å, d = 150Å (dotted) and l = 40Å, d = 180Å (solid). The comparison shows the different effect on the reflections width according to the arm orientations and dimensions.

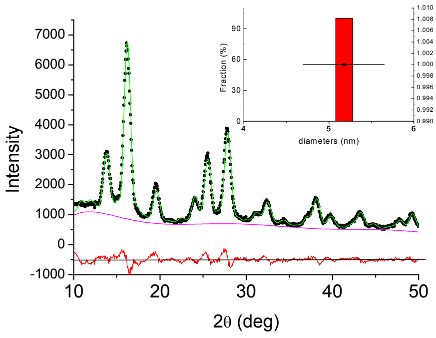

Fig. 4. *Iron oxide XRPD experimental dataset and relative calculated pattern. Background and difference profiles are included. Size & Strain distribution are shown in the inset. GoF = 2.43, Rwp = 6.79.*

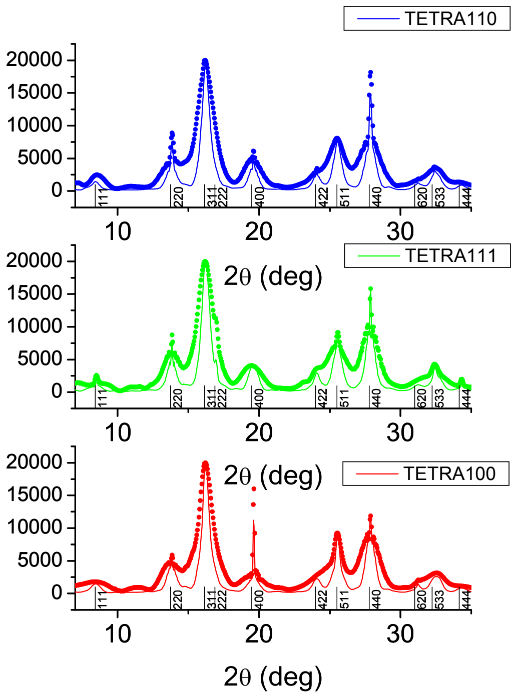

Fig. 5. *Calculated patterns for TPs with arms oriented along the [110], [111] and [100] orientations***.**

The increase of the I_{440}/I_{311} ratio as well as the (111) and (220) peak shift to higher angles, experimentally found, can be explained by a coexistence of TPs oriented both along the [111] and the [110], ruling out the [100] one. Tetrapods had been found with arms preferentially oriented along the [111] directions by transmission electron microscopy (TEM). Therefore, XRPD analysis confirmed TEM findings but adding a precious information.

PERSPECTIVES

Nowadays, the size and shape evolution of colloidal nanocrystals, driven by both thermodynamic parameters and kinetically-limited growth processes, is attempting to assemble different materials together in heterostructures (hybrid materials) playing with crystal miscibility, interfacial strain, and face-selective reactivity. The structural and compositional control of the resulting architecture is fundamental. Therefore powerful structural investigation tools are highly required. It is worth noting that fairly large amounts of material are produced and have to be controlled. In this respect, powder diffraction analysis has been showing to grant a rapid and cheap answer in terms of size, strain, shape and structure characterization. Relative data treatment methodologies are in continuous development and improvement to guarantee the most complete and reliable information. Critical aspects are the treatment of exotic shapes as well as the occurrence of defects. Further work is in progress to extend and complete the present theoretical approach.

The most important parts of software – as a program suite – are to be made available under GPL (Gnu Public License).

REFERENCES

* On leave from the Istituto di Cristallografia -CNR- Bari, Italy

[1] R. Lamber, S. Wetjen, I. Jaeger, *Phys. Rev.* **B 51** (1995) 10968.

[2] http://cst-www.nrl.navy.mil/lattice/prototype.html

[3] F.L. Ten Eyck, *Acta Cryst.* **A33** (1977) 486.

[4] A. Cervellino, C. Giannini, A. Guagliardi, *J. Appl. Cryst.* **36** (2003) 1148.

[5] A. Cervellino, C. Giannini, A. Guagliardi, *J. Comp. Chem.* **27** (2006) 998.

[6] A. Cervellino, C. Giannini, A. Guagliardi, *CPD Newsletter 30* (2005).

[7] L. Cademartiri, E. Montanari, G. Calestani, A. Migliori, A. Guagliardi, G.A. Ozin, *J. Amer. Chem.* Soc. (2006) in press.

[8] A. Cervellino, C. Giannini, A. Guagliardi, M. Ladisa, *Phys. Rev.* **B 72** (2005) 035412.

[9] P.D. Cozzoli, E. Snoeck, M.A. Garcia, C. Giannini, A. Guagliardi, A. Cervellino, F. Gozzo, A. Hernando, K. Achterhold, F.G. Parak, R. Cingolani, L. Manna, *Nanoletters* **6** (2006) 1966.

PRACTICAL ASPECTS OF PARTIAL COHERENCE OF NANOCRYSTALLINE DOMAINS

*David Rafaja, Volker Klemm and Milan Dopita**

Institute of Materials Science, TU Bergakademie Freiberg, Gustav-Zeuner-Str. 5, D-09599 Freiberg, Germany, E-mail: rafaja@ww.tu-freiberg.de

ABSTRACT

Partial coherence of crystallites is often observed in supra-hard nanocomposites having a strong texture as an effect causing the diffraction line “narrowing”. The degree of the partial coherence depends on the crystallite size, on the local preferred orientation of crystallites and on the size of the diffraction vector. Consequently, the microstructure parameters influencing the partial coherence of crystallites can be determined from the dependence of the diffraction line broadening on the size of the diffraction vector. In some thermodynamically unstable systems, like in Ti-Al-Si-N and Cr-Al-Si-N thin films, the strongly correlated orientation of adjacent crystallites that is a necessary condition for their partial coherence can be understood as an indicator of the spinodal decomposition.

INTRODUCTION

Nanocrystalline materials are employed in many industrial applications, e.g. in materials for catalytic converters, in production of self cleaning surfaces, in magnetic nanostructures or in supra-hard nanocomposites. Nano-sized structures combine advantages of excellent chemical and physical properties that are tailored by modification of the material’s microstructure. For these reasons, the microstructure analysis on nanocrystalline materials and nanocomposites is a very important issue for materials science. Obligatory methods for the microstructure analysis on nano-sized structures are the transmission electron microscopy (TEM) and the high-resolution transmission electron microscopy (HRTEM). The X-ray diffraction (XRD) offers still some benefits, the non-destructivity, a fast and easy sample preparation, and excellent statistics being few of them. Thus, XRD is still regarded as a very important experimental method for the microstructure analysis on nanocrystalline materials and nanocomposites [1 – 9].

X-RAY SCATTERING ON NANOCRYSTALS

Within the kinematical diffraction theory, the diffracting volume of a material under study is assumed to consist of individual coherently diffracting domains called crystallites. The X-ray scattering on atomic structures is usually described by the amplitude of the scattered wave, E, which is equal to the Fourier transformation (FT) of the electron density $\rho(\vec{r})$:

$$E(\vec{q})=\int_V \rho(\vec{r})\exp(i\vec{q}\cdot\vec{r})d\vec{r}=\mathrm{FT}[\rho(\vec{r})], \qquad (1)$$

where $\vec{q}$ is the diffraction vector and $\vec{r}$ the positions of the scattering centres. Electron density of an infinite crystal can be described as a convolution of the electron density of the unit cell $\rho_{\mathrm{cell}}(\vec{r})$ with the lattice function $L(\vec{r})$, see, e.g. [10]:

$$\rho_\infty(\vec{r})=\rho_{\mathrm{cell}}(\vec{r})*L(\vec{r}), \qquad (2)$$

where

$$L(\vec{r})=\sum_{n_1,n_2,n_3=-\infty}^{\infty}\delta\left(\vec{r}-\vec{r}_{n_1,n_2,n_3}\right). \qquad (3)$$

In Eq. (3), δ means the Dirac delta function, n_1, n_2 and n_3 are integers. Analogously, the electron density of an individual crystallite $\rho_{\mathrm{Xtal}}(\vec{r})$ can be described by convolution the electron density of the unit cell $\rho_{\mathrm{cell}}(\vec{r})$ with the lattice function $L(\vec{r})$ multiplied by a shape function $\Omega(\vec{r})$:

$$\rho_{\mathrm{Xtal}}(\vec{r})=\rho_{\mathrm{cell}}(\vec{r})*[\Omega(\vec{r})\cdot L(\vec{r})] \qquad (4)$$

$\Omega(\vec{r})$ is equal to unity within the crystallite and zero outside. The amplitude of the wave scattered by the crystallite is then given by the Fourier transformation of the electron density $\rho_{\mathrm{Xtal}}(\vec{r})$:

$$\begin{aligned}E(\vec{q})&=\mathrm{FT}[\rho_{\mathrm{Xtal}}(\vec{r})]=\mathrm{FT}\{\rho_{\mathrm{cell}}(\vec{\mathrm{r}})*[\Omega(\vec{r})\cdot L(\vec{r})]\}=\\&=\mathrm{FT}[\rho_{\mathrm{cell}}(\vec{r})]\cdot\mathrm{FT}[\Omega(\vec{r})\cdot L(\vec{r})]\end{aligned} \qquad (5)$$

The last term in Eq. (5), $\mathrm{FT}(\Omega\cdot L)$, describes the shape of three-dimensionally periodic reciprocal lattice points that are broadened due to the finite crystallite size. The Fourier transformation of the electron density of a unit cell is equal to the structure factor, which in the first approximation can be treated as a constant within the size of individual reciprocal lattice points:

$$\mathrm{FT}[\rho_{\mathrm{cell}}(\vec{r})]=F(\vec{q})\approx F(hk\ell) \qquad (6)$$

Within one reciprocal lattice point, the amplitude of the wave scattered by a finite crystallite is consequently given by a product of the structure factor of the unit cell and the Fourier transformation of the shape factor:

$$E(\vec{q})=F(hk\ell)\cdot\mathrm{FT}[\Omega(\vec{r})] \qquad (7)$$

The intensity scattered by the diffracting volume of material is proportional to the modulus of the sum of the amplitudes of waves scattered by individual crystallites (domains):

$$I(\vec{q})\propto\sum_{n=1}^{N}\left[F_{hk\ell}\cdot\mathrm{FT}(\Omega)\right]_n^*\cdot\sum_{n=1}^{N}\left[F_{hk\ell}\cdot\mathrm{FT}(\Omega)\right]_n \qquad (8)$$

Asterisk in Eq. (8) denotes the complex conjugate. The summation is performed over all crystallites within the irradiated volume of the sample. The product of the sums in Eq. (8) can easily be rewritten into the following form, which is more suitable for explaining the coherence phenomena in nanocrystalline materials:

$$\begin{aligned}I(\vec{q})\propto&\sum_{n=1}^{N}\left[F_{hk\ell}\cdot\mathrm{FT}(\Omega)\right]_n^*\cdot\left[F_{hk\ell}\cdot\mathrm{FT}(\Omega)\right]_n+\\&+2\sum_{m=1}^{N-1}\sum_{n=1}^{N-m}\left[F_{hk\ell}\cdot\mathrm{FT}(\Omega)\right]_n^*\cdot\left[F_{hk\ell}\cdot\mathrm{FT}(\Omega)\right]_{n+m}\end{aligned} \qquad (9)$$

The first term in Eq. (9) describes the scattering of X-rays on identical domains, i.e. the interference of waves scattered by the same crystallites. The second term describes the interference of waves scattered by different crystallites; the distance of the crystallites is hidden in the index m. Within the kinematical diffraction theory, different crystallites are assumed to be mutually non-coherent, thus the second term is neglected. This is valid only if

$$\left[F_{hk\ell} \cdot \mathrm{FT}(\Omega)\right]_n^* \cdot \left[F_{hk\ell} \cdot \mathrm{FT}(\Omega)\right]_m = 0 \qquad (10)$$

for n, $m = 1, \ldots, N$ and $n \neq m$, i.e. if the broadened reciprocal lattice points (from different crystallites) do not overlap each other.

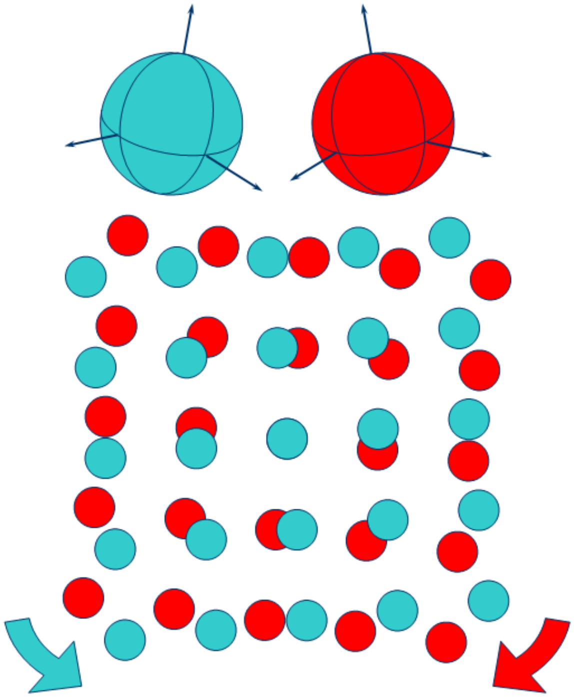

Fig. 1. *Effect of the mutual disorientation of crystallites on the rotation of their reciprocal lattices. The overlap of the reciprocal lattice points from different crystallites decreases with their increasing distance from the origin of the reciprocal lattice.*

A possible overlap of the reciprocal lattice points can be elucidated on the scheme shown in Fig. 1. Mutual rotation of crystallites causes opposing rotation of their reciprocal lattices around the origin of the reciprocal space. For small disorientations of nanocrystallites, i.e. crystallites having extremely broad reciprocal lattice points, some reciprocal lattice points do overlap partially (Fig. 1). This overlap can be understood as partial coherence of the crystallites. For two partially coherent crystallites, the intensity is given by the modulus of the sum of amplitudes of the waves scattered by individual crystallites, see Eq. (9):

$$I \propto \left|E_1 + E_2\right|^2 = \left|E_1\right|^2 + 2\,\mathrm{Re}\left(E_1^* E_2\right)\left|\Gamma_{12}\right| + \left|E_2\right|^2 \qquad (11)$$

Mutual shift of crystallites modifies the phase φ of the amplitudes scattered by the respective crystallites,

$$E_1 = \left|E_1\right| \exp\left(i\varphi_1\right) \text{ and } E_2 = \left|E_2\right| \exp\left(i\varphi_2\right), \qquad (12)$$

which takes effect on the “mixed” middle term in Eq. (11). Using Eq. (12), equation (11) can be rewritten into the following form:

$$I \propto \left|E_1\right|^2 + \left|E_2\right|^2 + 2\left|E_1\right|\left|E_2\right| \cos\left(\varphi_1 - \varphi_1\right)\left|\Gamma_{12}\right| \qquad (13)$$

The phase difference $\left(\varphi_1 - \varphi_2\right)$ is given by the scalar product of $\vec{q}$ and $\vec{R}$, where $\vec{R}$ is the distance between the two crystallites involved in the scattering process. The parameter Γ_{12} occurring in equations (11) and (13) characterises the degree of coherence of the radiation [11], which is related to the coherence length of the radiation in the longitudinal direction [12] that can be calculated from the Heisenberg uncertainty relation:

$$\Lambda = \frac{\lambda^2}{2\Delta\lambda} \qquad (14)$$

The coherence length of the CuKα_1 radiation emitted by a sealed X-ray tube ($\lambda = 1.54056$ Å, $\Delta\lambda = 3.615 \times 10^{-4}$ Å) is approximately 0.33 µm, which is sufficient to accommodate up to a hundred of neighbouring nanocrystallites within the coherence length.

Another parameter influencing the degree of the coherence of adjacent crystallites is the product of $|E_1|$ and $|E_2|$ in Eq. (13). As discussed above, this product is non-zero only if the reciprocal lattice points from these crystallites are overlapping each other. Figures 2, 3 and 4 illustrate the effect of the overlap of the reciprocal lattice points on the shape of the two-dimensional intensity maxima in form of the $\Delta q_x/\Delta q_z$-scans. Δq_x is proportional to the crystallite's disorientation; Δq_z denotes the distance from the diffraction maximum. In the microstructure model used for simulation of the partial coherence phenomena that are shown in Figures 2 – 4, spherical crystallites were displaced along the z direction. Their displacement was equal to their size, which means that the crystallites were assumed to be in direct contact. For spherical crystallites, the Fourier transform of the shape factor is given by the equation:

$$\mathrm{FT}\left[\Omega(\vec{q})\right] = \int\limits_{\text{Sphere}} \exp\left(i\vec{q}\cdot\vec{r}\right) d\vec{r} = \qquad$$

$$= \frac{4\pi}{|\vec{q}|^2}\left(\frac{\sin|\vec{q}|R}{|\vec{q}|} - R\cos|\vec{q}|R\right), \qquad (15)$$

where R is the radius of the sphere and

$$|\vec{q}| = \frac{4\pi}{\lambda}\sin\theta \qquad (16)$$

the size of the diffraction vector. In a polycrystalline material consisting of pairs of partially coherent crystallites, the reciprocal lattice points shown in Figures 2 – 4 are distributed along a sphere, for which $|\vec{q}| = \text{const}$. This distribution corresponds to different orientations of the pairs of partially coherent crystallites. Regarding the resolution of a diffractometer in the q_x direction, the registered intensity is, in fact, integrated over a broad q_x range:

$$I \approx \int\left[\left|E_1\right|^2 + \left|E_2\right|^2 + 2\left|E_1\right|\left|E_2\right|\cos\left(\vec{q}\cdot\vec{R}\right)\right] dq_x \qquad (17)$$

and depends consequently only on q_z.

According to Eq. (7), the amplitudes E_1 and E_2 are given by the Fourier transformations of the shape factors of the disoriented crystallites that follow, for spherical crystallites with the radius R, from Eq. (15).

$$\begin{aligned} E_1 &= FT\left[\Omega(\vec{q}+\Delta\vec{q})\right] = \\ &= \frac{4\pi}{\left|\vec{q}+\Delta\vec{q}\right|^2}\left(\frac{\sin\left|\vec{q}+\Delta\vec{q}\right|R}{\left|\vec{q}+\Delta\vec{q}\right|} - R\cos\left|\vec{q}+\Delta\vec{q}\right|R\right) \end{aligned} \tag{18}$$

$$\begin{aligned} E_2 &= FT\left[\Omega(\vec{q}-\Delta\vec{q})\right] = \\ &= \frac{4\pi}{\left|\vec{q}-\Delta\vec{q}\right|^2}\left(\frac{\sin\left|\vec{q}-\Delta\vec{q}\right|R}{\left|\vec{q}-\Delta\vec{q}\right|} - R\cos\left|\vec{q}-\Delta\vec{q}\right|R\right) \end{aligned} \tag{19}$$

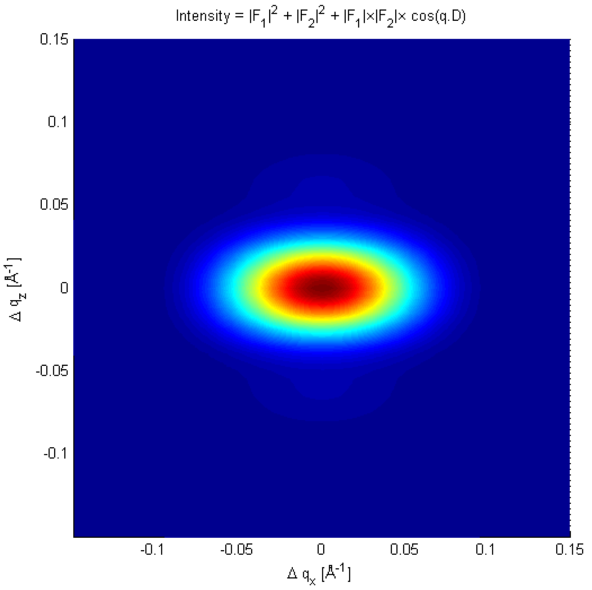

Fig. 2. *Two-dimensional intensity distribution as calculated using Eqs. (7), (13) and (15) for fully coherent crystallites having the size of 30 Å. The reciprocal lattice points were completely overlapping each other.*

Consequently, the radial intensity distribution, i.e. the dependence of the intensity on q_z, depends strongly on the degree of the partial coherence of crystallites, which is hidden in the coherence term of Eq. (17). The change of the line broadening and the change of the line shape are illustrated in Fig. 5. For non-coherent crystallites (Fig. 4), the scattered intensity corresponds to the sum of the intensities scattered by individual crystallites. Thus, the line width and the line shape remain the same as for individual crystallites, like in the classical kinematical diffraction theory. For fully coherent crystallites replaced in the z direction, the scattered intensity (Fig. 2) is modulated additionally by the cosine term from Eq. (17) in the q_z direction, which causes an obvious decrease of the line broadening in this direction (Fig. 5). For partially coherent crystallites (Fig. 3), the line broadening along q_z lies between the line broadening from fully coherent and non-coherent crystallites. Moreover, the diffraction lines from partially coherent crystallites become Cauchy-like in shape due to their long tails in the q_z direction, see Fig. 3.

DIFFRACTION LINE BROADENING

In [6], we have shown that the diffraction line broadening from partially coherent crystallites can be divided into three regions that are shown in Fig. 6. For $\sin\theta \to 0$, the diffraction line broadening is given by the maximum size of domains, which consist of several partially coherent crystallites. At medium diffraction angles, the diffraction line broadening steeply increases with increasing diffraction angle as the degree of the partial coherence (as well as the overlap of the reciprocal lattice points, see Fig. 1) decreases in this range.

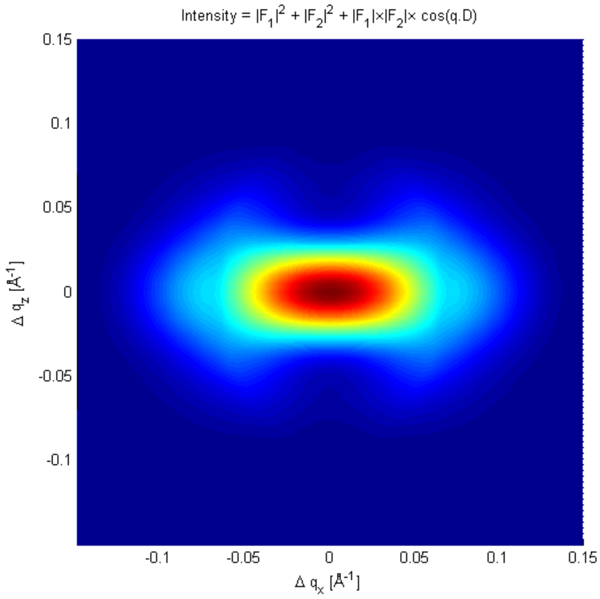

Fig. 3. *Two-dimensional intensity distribution as calculated using Eqs. (7), (13), (15) for partially coherent crystallites having the size of 30 Å. The distance of the reciprocal lattice points was 0.09 Å^{-1} along q_x.*

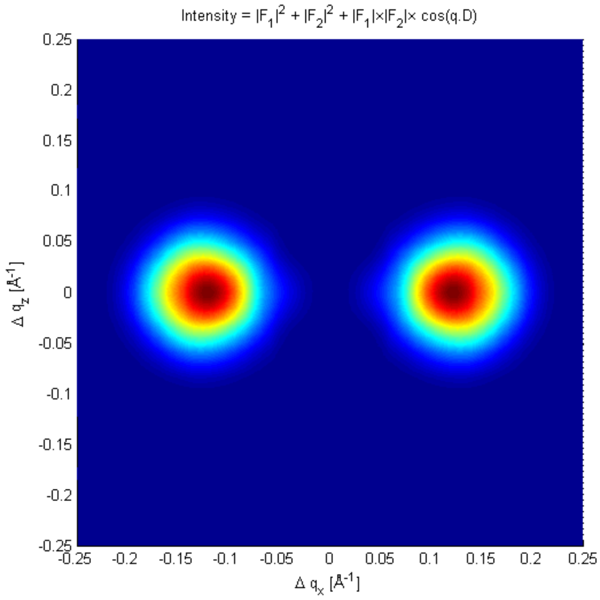

Fig. 4. *Two-dimensional intensity distribution as calculated using Eqs. (7), (13), (15) for non-coherent crystallites having the size of 30 Å. The distance of the reciprocal lattice points was 0.15 Å^{-1} along q_x.*

At the largest diffraction angles, the reciprocal lattice points do not overlap, which means that the coherence of neighbouring crystallites disappears completely. In this angular range, the diffraction line broadening remains constant, being approximately equal to the reciprocal size of individual (non-coherent) crystallites.

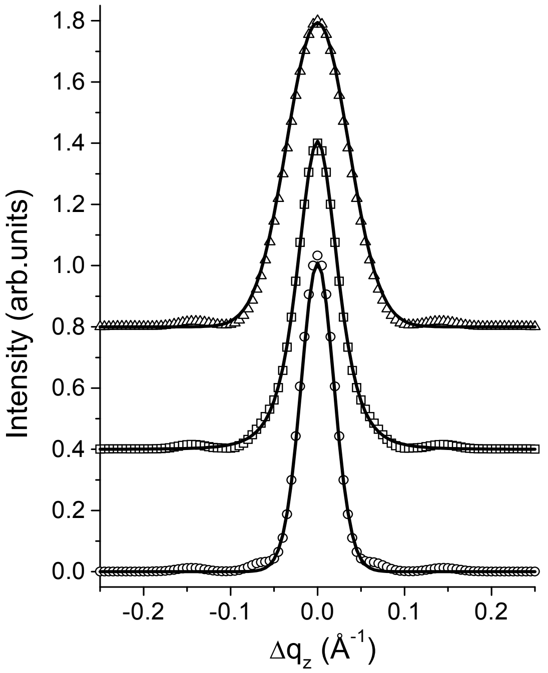

Fig. 5. *Diffraction profiles calculated using equations (17), (18) and (19) for incoherent, partially coherent and fully coherent crystallites (from the top to the bottom). The displacement of the reciprocal lattice points is the same like in Figures 4, 3 and 2, respectively.*

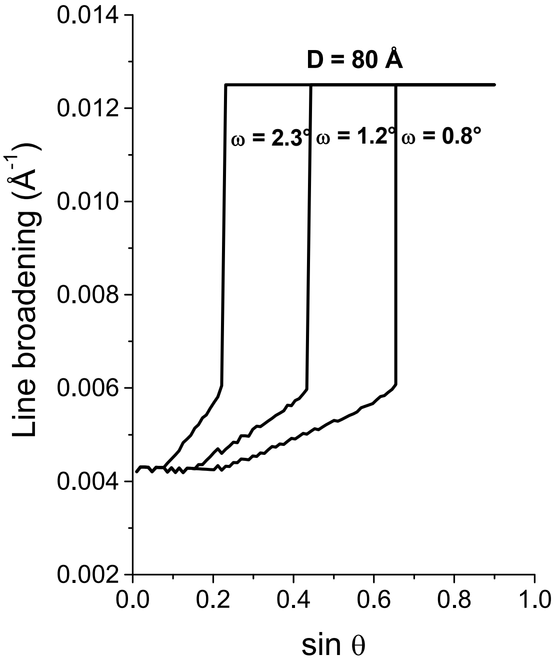

Fig. 6. *Diffraction line broadening as calculated according to Ref. [6] for partially coherent crystallites with the size of 80 Å and with the disorientation of 0.8°, 1.2° and 2.3°. Small oscillations in the range of the increasing line broadening are due to the numerical errors.*

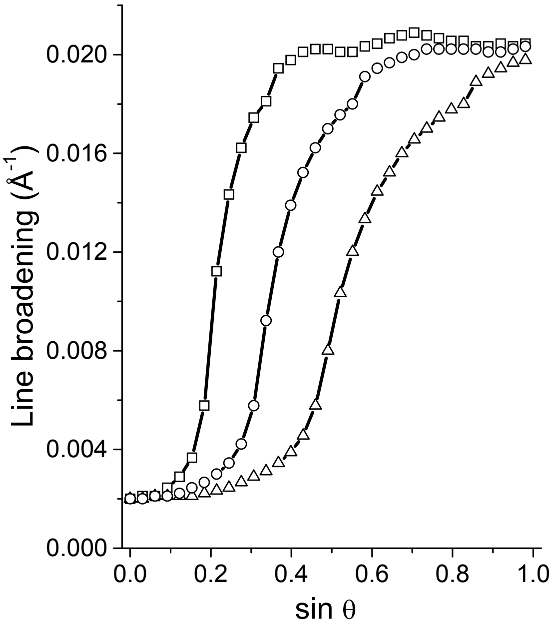

Fig. 7. *Diffraction line broadening as calculated according to equations (17), (18) and (19) for partially coherent crystallites with the size of 50 Å and with the disorientation of 1.0° (triangles), 1.5° (circles) and 2.5° (boxes).*

An analogous dependence of the diffraction line broadening on the diffraction angle can also be derived using the approach described in the previous Section. The line broadening shown in Fig. 7 was obtained from fitting the diffraction profiles calculated using equations (17), (18) and (19) by the Pearson VII function. Some examples of the line profile fitting are shown in Fig. 5. In both approaches discussed above, the minimum and the maximum diffraction line broadening correspond to the size of clusters of partially coherent crystallites and to the size of non-coherent crystallites, respectively. The main difference between these approaches is the steepness of the increase of the diffraction line broadening with increasing diffraction angle. The microstructural model described in [6] assumes a continuous distribution of the disorientations of neighbouring crystallites between zero and a maximum disorientation, which increases the degree of the coherence in the middle range of the diffraction angles and shifts the steep increase of the diffraction line broadening to larger diffraction angles. Consequently, the higher degree of the partial coherence of crystallites in the middle range of the diffraction angles causes a steeper increase of the diffraction line broadening at larger diffraction angles. The other microstructural model, which was used for the approach described in the previous Section, assumes a constant disorientation of neighbouring crystallites in the clusters of partially coherent crystallites, which leads to a gradual decay of the partial coherence of crystallites that is demonstrated by a slower increase of the diffraction line broadening with increasing diffraction angle. These two approaches characterise approximately the limit cases of the scattering on partially coherent crystallites.

EXPERIMENTAL EXAMPLES

For the first time, the coherence of nanocrystalline domains was observed in the Ti-Al-N [6, 9] and Ti-Al-Si-N [9] nanocomposites, for which the spinodal decomposition was reported [13 – 16]. Recently, we observed the partial coherence of nanocrystallites in the Cr-Al-Si-N nanocomposites [17]. The relationship between the spinodal decomposition and the partial coherence of crystallites was discussed in [9] on the example of the Ti-Al-N and Ti-Al-Si-N systems. A requirement for the partial coherence of nanocrystallites is their small disorientation (see Figures 1, 2, 3, 6 and 7). The maximum amount of the disorientation of coherent nanocrystallites depends both on their size and on the minimum distance of the reciprocal lattice points from the origin of the reciprocal space, i.e. on the lattice parameter and the lattice type, but it typically does not exceed 3°. Ti-Al-N and Ti-Al-Si-N nanocomposites contain fcc-(Ti, Al) N phase with the NaCl structure and hexagonal AlN phase with the wurtzitic structure. As we have shown in [9], a very strong local preferred orientation of crystallites can be transferred between cubic crystallites through the hexagonal phase as some interplanar distances are similar in these particular crystal structures.

Two examples illustrating the partial coherence of nanocrystallites in the Cr-Al-Si-N nanocomposites having the chemical compositions $\mathrm{Cr_{0.40}Al_{0.52}Si_{0.08}N}$ and $\mathrm{Cr_{0.91}Al_{0.08}Si_{0.01}N}$ are shown in Fig. 8. The simulation of the line broadening for partially coherent crystallites was performed using the routine described in [6] and is shown by solid lines in Fig. 8. For the sample $\mathrm{Cr_{0.40}Al_{0.52}Si_{0.08}N}$, the simulation yielded the crystallite size of (47 ± 3) Å. The disorientations of crystallites are larger than 3° as estimated from the position of the steep increase of the line broadening with increasing diffraction angle; the crystallites are non-coherent in the accessible range of the diffraction angles. The crystallite size was verified by transmission electron microscopy with high resolution (HRTEM), see Fig. 9. The dependence of the diffraction line broadening on the size of the diffraction vector measured for the $\mathrm{Cr_{0.91}Al_{0.08}Si_{0.01}N}$ nanocomposite indicated clearly the partial coherence of neighbouring crystallites. From the size of the diffraction vector, for which the steep increase of the line broadening was observed, and from the maximum (saturated) line broadening, the mean disorientation of crystallites of (0.6 ± 0.1)° and the crystallite size of (117 ± 7) Å was determined, respectively. From extrapolation of the diffraction line broadening to $\sin\theta = 0$ (dashed line in Fig. 8), the size of the partially coherent domains was estimated to be between 500 and 600 Å.

Thus, it can be concluded that the sample with the chemical composition $\mathrm{Cr_{0.91}Al_{0.08}Si_{0.01}N}$ consists of small slightly disoriented crystallites that create large blocks containing 4 – 5 small partially coherent crystallites. Large blocks are mutually strongly disoriented and therefore non-coherent. The microstructure of this sample is illustrated by the HRTEM micrograph in Fig. 10. One large block can be seen in the middle of the picture. It consists from several small partially coherent crystallites (dark regions in Fig. 10). Small disorientation of the partially coherent crystallites was confirmed by the presence of the moiré pattern [18].

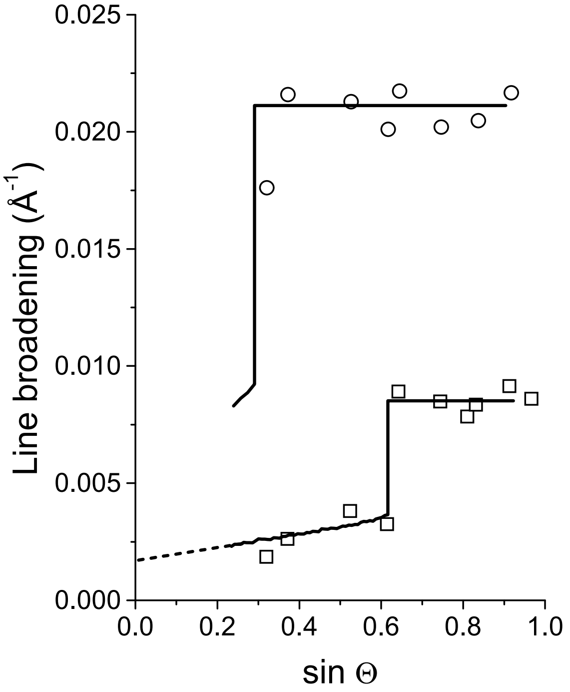

Fig. 8. *Diffraction line broadening observed in samples* $\mathrm{Cr_{0.40}Al_{0.52}Si_{0.08}N}$ *(circles) and* $\mathrm{Cr_{0.91}Al_{0.08}Si_{0.01}N}$ *(boxes) [17]. The instrumental line broadening measured using the* $\mathrm{LaB_6}$ *standard from NIST was subtracted from the experimental data.*

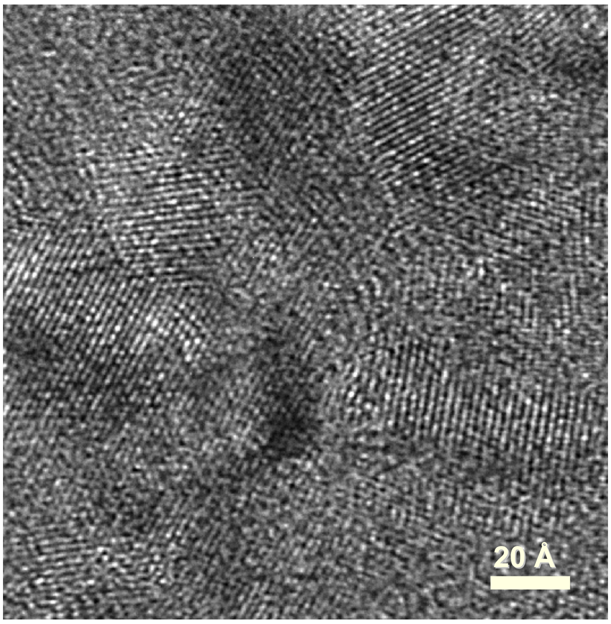

Fig. 9. *HRTEM micrograph of the sample with the overall chemical composition* $\mathrm{Cr_{0.40}Al_{0.52}Si_{0.08}N}$.

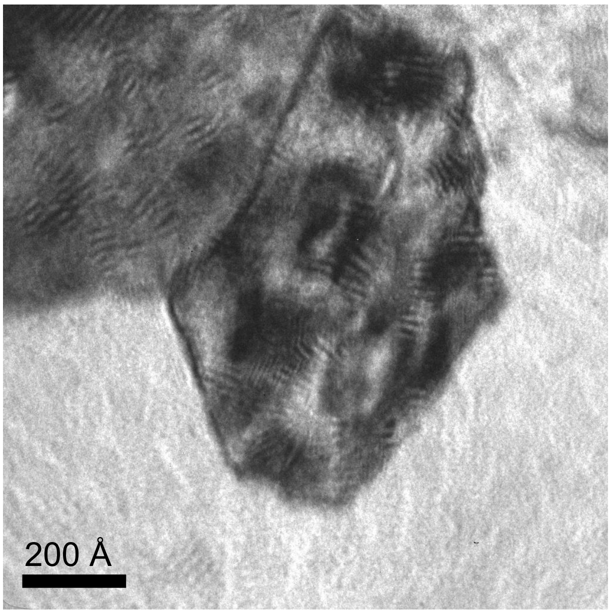

Fig. 10. *HRTEM micrograph of the sample with the overall chemical composition* $Cr_{0.91}Al_{0.08}Si_{0.01}N$.

CONCLUSIONS

It was shown that broad reciprocal lattice points from nanosized crystallites can overlap each other. This overlap of the reciprocal lattice points reduces the broadening of the diffraction lines as seen by X-ray diffraction. In the direct space, the overlap of the reciprocal lattice points is equivalent to the partial coherence of adjacent crystallites that "enlarges" their size as seen by X-rays. As the overlap of the reciprocal lattice points decreases with increasing size of the diffraction vector, the effect of the partial coherence of crystallites on the line broadening varies with the diffraction angle, which can be used to obtain the following microstructural information from the XRD line broadening.

- Size of individual partially coherent crystallites can be calculated from the maximum (saturated) diffraction line broadening observed for large diffraction angles.
- Mean local disorientation of the individual partially coherent neighbouring crystallites is related to the size of the diffraction vector, for which the partial coherence of crystallites disappears.
- Size of the blocks composed of individual partially coherent crystallites can be estimated from the extrapolation of the diffraction line broadening to $q = 0$.

The partial coherence of neighbouring crystallites was observed in materials consisting of nanocrystalline domains with a strong local preferred orientation of crystallites. Nanocrystalline domains are necessary for getting broadened reciprocal lattice points; strong local texture is needed for a sufficient overlap of the reciprocal lattice points from neighbouring crystallites. The last requirement for the partial coherence of nanocrystallites is that the distance of such nanocrystallites must be smaller than the coherence length of the X-rays used for the experiment, which is a general optical requirement for interference of scattered waves.

ACKNOWLEDGEMENTS

The authors appreciate the financial support of the project number RA-1050/9-1 through the German Research Council (DFG). The HRTEM JEM 2010 FEF was financed through DFG in the frame of the Priority program number 1062. Furthermore, we thank Dr. M. Šíma and M. Růžička (SHM Ltd., Šumperk, Czech Republic) for providing us with samples of the Ti-Al-Si-N and Cr-Al-Si-N thin films nanocomposites.

REFERENCES

* On leave from the Department of Condensed Matter Physics, Faculty of Mathematics and Physics, Charles University Prague, Czech Republic

[1] R.L. Snyder, J. Fiala, H.J. Bunge: *Defect and Microstructure Analysis by Diffraction*, Oxford University Press, 1999.

[2] N. Guillou, J.P. Auffrédic, D. Louër, *Powder Diffraction* **10** (1995) 236.

[3] J.I. Langford, D. Louër, P. Scardi, *J. Appl. Cryst.* **33** (2000) 964.

[4] A. Cervellino, C. Giannini, A. Guagliardi, *J. Appl. Cryst.* **36** (2003) 1148–1158.

[5] D. Rafaja, M. Šíma, V. Klemm, G. Schreiber, D. Heger, L. Havela, R. Kužel, *J. Alloys Comp.* **378** (2004) 107.

[6] D. Rafaja, V. Klemm, G. Schreiber, M. Knapp, R. Kužel, *J. Appl. Cryst.* **37** (2004) 613.

[7] G. Ribárik, N. Auderbrand, H. Palancher, T. Ungár, D. Louër, *J. Appl. Cryst.* **38** (2005) 912.

[8] A. Cervellino, C. Giannini, A. Guagliardi, M. Ladisa, *Phys. Rev.* **B72** (2005) 035412.

[9] D. Rafaja, A. Poklad, V. Klemm, G. Schreiber, D. Heger, M. Šíma, M. Dopita, *Thin Solid Films* **514** (2006) 240-249.

[10] C. Giacovazzo, H.L. Monaco, G. Artioli, D. Viterbo, G. Feraris, G. Gilli, G. Zanotti, M. Catti: *Fundamentals of Crystallography*, 2nd Edition, IUCr Texts on Crystallography 7, Oxford University Press, 2002.

[11] M. Born, E. Wolf: *Principles of Optics*, 7th Edition, University Press, Cambridge, 1999.

[12] U. Pietsch, V. Holý, T. Baumbach: *High-Resolution X-Ray Scattering – From Thin Films to Lateral Nanostructures*, Springer, Berlin, 2004.

[13] H.-D. Männling, D.S. Patil, K. Moto, M. Jílek, S. Veprek, *Surf. Coat. Technol.* **146** (2001) 263.

[14] A.E. Santana, A. Karimi, V.H. Derflinger, A. Schutze, *Thin Solid Films* **469** (2004) 339.

[15] A. Hörling, L. Hultman, M. Odén, J. Sjölén, L. Karlsson, *Surf. Coat. Technol.* **191** (2005) 384.

[16] A. Flink, T. Larsson, J. Sjölen, L. Karlsson, L. Hultman, *Surf. Coat. Technol.* **200** (2005) 1535.

[17] D. Rafaja, M. Dopita, M. Růžička, V. Klemm, D. Heger, G. Schreiber, M. Šíma, *Surf. Coat. Technol.* **201** (2006) 2835-2843.

[18] D.B. Williams, C.B. Carter: *Transmission Electron Microscopy III – Imaging*, Plenum Press, New York, 1996.

THE MICROSTRUCTURE OF NANOCRYSTALLINE MATERIALS DETERMINED BY X-RAY LINE PROFILE ANALYSIS

Tamás Ungár

Department of Materials Physics, Institute of Physics of the Eötvös University Budapest, P.O.Box 32, H-1518 Budapest, Hungary, E-mail: ungar@ludens.elte.hu

INTRODUCTION

X-ray line profile analysis (XLPA) is a powerful tool for characterising the microstructure of crystalline materials in terms of size and strain [1-28]. It has the advantage to provide average values of physically relevant parameters. However, often the appropriate interpretation needs the assistance of other methods, especially the electron microscopy. The concomitant application of XLPA and different electron microscopic methods, e.g. transmission or scanning electron microscopy (TEM or SEM), or electron back-scatter diffraction (EBSD) provides probably the best complex microstructure characterisation. The most straightforward microstructure properties obtained by XLPA are the (i) average crystallite size and (ii) size distribution, (iii) average dislocation density and (iv) the character of dislocations, (v) slip activity, (vi) active Burgers vectors and (vii) planar defect densities, or (viii) different types of internal stresses of first and second order, (ix) and long-range-internal stresses prevailing in heterogeneous microstructures.

Nanocrystalline materials can either be in the form of loose powders or compact bulk materials, ceramics, ionic crystals or metals and they can have been produced by different methods. XLPA has the great advantage that it can be applied for all different types of materials irrespective of synthesis or constitution. The microstructure of this type of materials can be divided into two fundamental features: (i) the grain or crystallite size and (ii) the structure of lattice defects.

The ideal powder diffraction pattern consists of narrow, symmetrical peaks at the exact Bragg positions. A number of different types of deviations from the ideal peak profile are conceivable: (*a*) peak shifts, (*b*) peak broadening, (*c*) peak asymmetries and (*d*) anisotropic broadening or peak shape, where the anisotropy is meant in terms of *hkl* dependence. There is no one-to-one correlation between the different peak profile features and the different microstructural properties. It is the experimentators skills and task to find the appropriate interpretation of X-ray line profiles. The game becomes more reliable if other methods, especially TEM, SEM or EBSD are also used. On the other hand, the results of these other methods, in particular the electron microscopy, can be refined or complemented by using XLPA.

SIZE AND SIZE-DISTRIBUTION IN NANOCRYSTALLINE MATERIALS

Nanocrystalline metals and alloys can be produced by many different methods, e.g. inert-gas condensation and subsequent hot compaction [10] and [15], ball milling [9, 13, 16], ball milling and hot iso-static pressure (HIP) [11], crystallization from the bulk amorphous state [28], different deposition methods [23], or by severe plastic deformation [8, 17, 31]. Size distribution of grains, sub-grains or crystallite size is readily available by the classical Warren-Averbach [1, 9, 10, 13], or the more recent whole-profile or whole-pattern modelling methods [17, 19, 24, 25, 31]. There is an ongoing search for the correlation between size values and size distributions determined either by TEM, SEM or EBSD and XLPA [9, 10, 15-17, 24, 27, 29 and 31]. As long as the coherently scattering domains have well determined boundaries, e.g. in the case of specimens prepared by ball milling or by compaction of nanoparticles, the good correlation is almost straightforward [9, 10, 11, 13, 15, 16 and 29]. In plastically deformed metals or alloys the correlation is not so trivial, since the boundaries in a TEM micrograph are (i) of very different types and (ii) the contrast in the micrographs depend on careful tilting exercises [29] and [33]. The log-normal size distribution functions of crystallites in inert-gas condensed and compacted nanocrystalline copper specimens determined by XLPA (short and long dash lines) and TEM (solid and dash-dot lines, and open symbols) [10] and [15] are shown in Fig. 1. A good correlation between the TEM and X-ray size distributions can be seen.

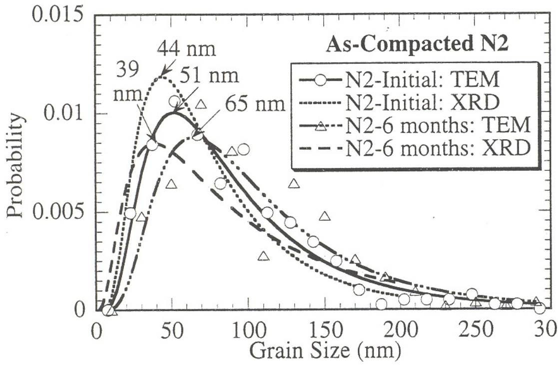

Fig. 1. *Comparison of the grain size distributions (number fraction) obtained by XLPA and TEM studies on inert-gas condensed and compacted nanocrystalline copper specimens in the as-compacted initial state (dotted and solid lines) and after 6 months at room temperature (dashed and dash-dotted lines), respectively. The arrows point to the median values of each distribution. (By courtesy of Mitra et al. [15]).*

In [29] it was shown that in bulk metallic materials prepared by plastic deformation the X-ray size and size-distributions correspond to the size of sub-grains in TEM micrographs. The size and size-distribution of crystallites in ceramic materials influence the kinetics of the sintering process and determine the density and the macroscopic properties of the material [35]. Several examples have shown that there is a good correlation between the size parameters provided by electron microscopy, the method of Brunauer–Emmett–Teller (BET) and XLPA [4, 13, 16, 18, 19, 21, 24, 27 and 36]. Deviations from spherical or globular shape cause anisotropies of line broadening in terms of *hkl* indices which has been treated readily by different numerical methods [4, 17, 37 and 38].

STRAIN IN NANOCRYSTALLINE MATERIALS

Strain in nanocrystalline materials is even a greater challenge than size. It is caused by lattice distortions and is directly linked to lattice defects. The fundamental parameter for describing strain is the mean-square-strain, $<\varepsilon^2>$, as defined by Warren [1]. The question is how to solve $<\varepsilon^2>$. Warren realized in the early fifties that for Gaussian strain distribution $<\varepsilon^2>$ would be constant. This, however, never occurs in reality. The mean-square-strain appears in the Fourier coefficients or transforms of peak profiles; therefore it is a function of the Fourier variable, L. Its L dependence is related to the spatial distribution of the deformation ε or the displacements $\boldsymbol{u}$ of atoms. In relation with line broadening there is another aspect of $<\varepsilon^2>$. The deformation ε can in principle be (i) of short range, (ii) of long range character or (iii) constant. In the first and second case, its spatial dependence is $1/r^2$ and $1/r$, respectively. For the third case, i.e. for ε = constant, the lattice deformation has no effect on the line broadening (at least in the present context), as it causes line shift. Due to reciprocity between the crystal space and the reciprocal space, short or long range character in deformation changes to its reciprocal in reciprocal space, i.e. in diffraction. This means that the short range character deformation will give scattering that is far from the fundamental Bragg reflections, whereas the long range character of deformation scattering that is close or even around the fundamental Bragg reflections. The scattering that is far from the fundamental Bragg reflections is diffuse scattering which is often included in the background. Only the scattering that is close or around the fundamental Bragg reflections is considered as *line broadening*. It is important to note that, though the contributions of diffuse scattering are reaching far from the fundamental Bragg reflections, their contributions are present in the entire reciprocal space. The formal classification of the spatial dependence of deformation and its relation to scattering is in close connection with the type of lattice defects [3, 6]. (1) Point defects, (2) small dislocation loops, (3) precipitates or inclusions cause deformations of short range character, and the corresponding scattering contributes to *diffuse scattering*. (4) Dislocations, (5) triple junctions of grain boundaries or (6) contact stresses between touching particles (also called sinter stresses) cause deformations of long range character, and the corresponding scattering clusters around the fundamental Bragg reflections. Only this type of scattering is considered as *strain broadening*. (7) Planar defects cause a homogeneous deformation that produces line shift, see also Section "Stacking faults and twinning". Wilkens calculated $<\varepsilon^2>$ for parallel screw dislocations in the entire L range [3]. Groma [39] has shown that this strain function and the corresponding strain profile have a far more general validity than just the model used by Wilkens. Since the physical nature of deformations caused by the other two lattice defect types, i.e. triple junctions and sinter stresses, are identical to that of dislocations, they cannot be distinguished by the line profile analysis. Therefore, the best what strain broadening can provide is a dislocation structure in terms dislocation density, ρ and the effective outer cut-off-radius, R_e, (or $M = R_e\rho^{1/2}$). The interpretation of these parameters in terms of true dislocations or the other two lattice defects (# 5 and 6 above) has to be done by using other methods, e.g. the electron microscopy.

THE INTERFERENCE PHENOMENON IN X-RAY DIFFRACTION FROM NANOCRYSTALLINE MATERIALS

The Williamson-Hall plot of the full width at half maxima (FWHM) of the diffraction peaks of a nanocrystalline thin film of $Ti_{0.38}Al_{0.62}N$ [23] is shown in Fig. 2 (see figure 6 in [23]). It can be seen that for small values of the diffraction vector (here the first 7 reflections) the peaks are narrower by almost an order of magnitude than the peaks at larger values of the diffraction vector.

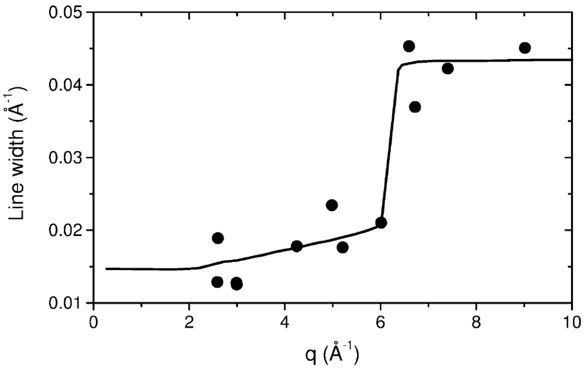

Fig. 2. *Williamson-Hall plot of the full width at half maxima (FWHM) of the diffraction peaks of a nanocrystalline thin film of $Ti_{0.38}Al_{0.62}N$ (full dots) and the simulation of the X-ray interference effect (solid line) (by courtesy of Rafaja et al. [23]).*

High resolution transmission electron microscopy (see figures 4 and 5 in [23]) has shown that the crystallite size correlates with the FWHM of the broader peaks at q values above 6 Å^{-1}. The narrowing of the peaks close to the origin of reciprocal space has been interpreted by the interference between scattering from adjacent crystallites with small orientation differences. The same effect was found in ball milled Fluorides for specific bal-milling periods, especially when the size distribution indicated that a relatively large volume fraction of crystallites are smaller than about 5 nm [40]. Fig. 3 shows the measured and fitted diffraction patterns of SrF_2 ball milled for 12 and 40 min, respectively. It can be seen that in the case of 12 min ball milling the measured and the model based fitting coincides over the intensity range of three orders of magnitude (note the logarithmic intensity scale). However, in the case of the specimen ball milled for 40 min the first 3 to 4 reflections are narrower than the fitted spectrum, whereas, the higher order reflections comply perfectly to the model based fitting. In order to see the effect clearly, only the first parts of the diffraction patterns up to about 2θ = 78° are shown here.

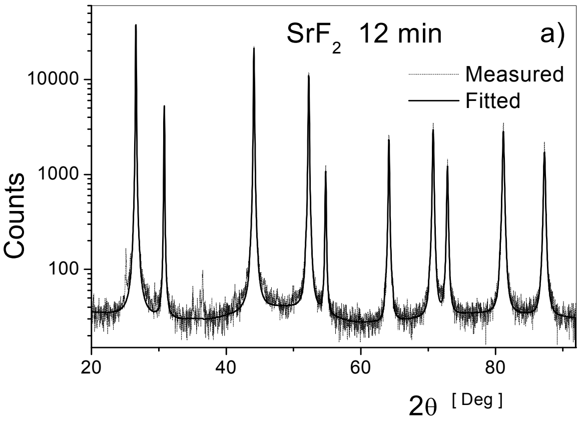

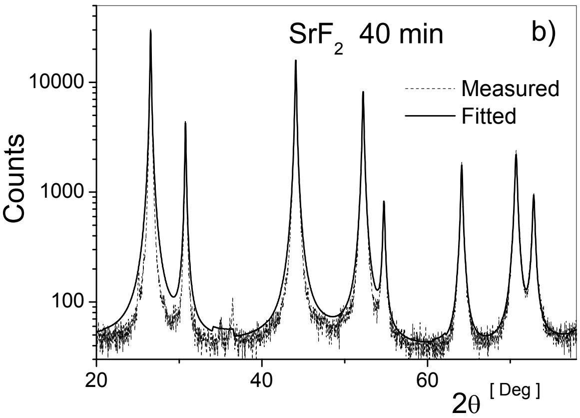

Fig. 3. *Observed (dotted line) and fitted (solid line) patterns of SrF_2 after 12 (a) and 40 (b) minutes ball milling. Note the logarithmic intensity scale. (By courtesy of Ribárik et al. [40])*

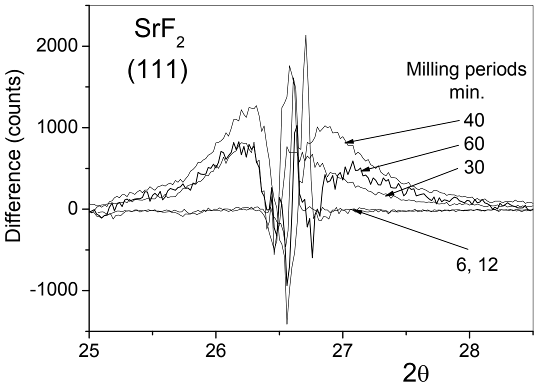

Fig. 4. *The difference between the measured and fitted intensities of the 111 Bragg reflection as a function of the period of ball milling of SrF_2. (By courtesy of Ribárik et al. [40].)*

In the case of the specimen ball milled for 60 min the measured and model based fitted patterns coincide again, as in the case of the 12 min ball milling. The appearing and disappearing of the interference effect with milling time is shown by plotting the difference between the measured and fitted intensities of the 111 Bragg reflections in Fig. 4. The positive deviations in the tail regions of the intensities indicate that the measured profiles are narrower than the fitted ones. The figure shows that the peak narrowing relative to the model peaks is negligible for 6 and 12 min, increases to a maximum at 40 min and decreases for longer ball milling periods, respectively. It is important to note that the coincidence of the measured and modelled intensities was found to be perfect for all measured diffraction patterns from the fourth or fifth Bragg reflections up to the last, fifteenth measured reflection. The size distribution of crystallites went through a minimum around 40 min ball milling, as it can be seen in Fig. 13 in [40]. The interference effect in the ball milled Fluorides has been interpreted as follows. A simple picture for the interference effect was given by figure 7 in [40] or figure 1 in [41]. It shows the schematic diffraction spots in reciprocal space blown up by small particle size for two adjacent crystallites with a small difference in their crystallographic orientation. The figure is reproduced here as Fig. 5. The interference effect occurs when two diffraction spots corresponding to adjacent crystallites overlap, cf. [23].

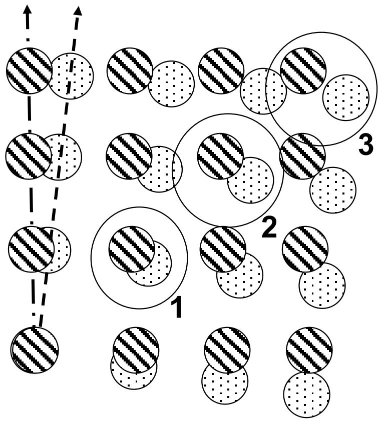

Fig. 5. *Schematic drawing for the interpretation of the interference effect. The dashed and the dotted spots are the blown up reciprocal lattice nodes corresponding to two adjacent crystallites rotated in orientation with respect to each other by a small angle. The orientations of the two crystallites are indicated schematically by the dashed and dash-dotted arrows. The two diffraction spots encircled and numbered 1 and 2 overlap, whereas the ones numbered 3 are well separated. (By courtesy of Ribárik et al. [40]) A similar figure can be found in [41].*

This can happen if (i) the crystallites are small, so that the blow up of diffraction spots is large, (ii) if the lattice constant of the material is large, so that there are diffraction spots not too far from the origin of reciprocal space and (iii) the orientation difference between adjacent crystallites is small enough, so that the overlap can occur. In the case of the ball milled Fluorides condition (i) is assured by ball milling. The lattice parameter of the Fluorides is somewhat larger than 0.5 nm, a relatively large value. The local texture in condition (iii) is conceivable since the specimens are ionic crystals and there might be a strong physical (Coulomb) interaction between touching crystallites.

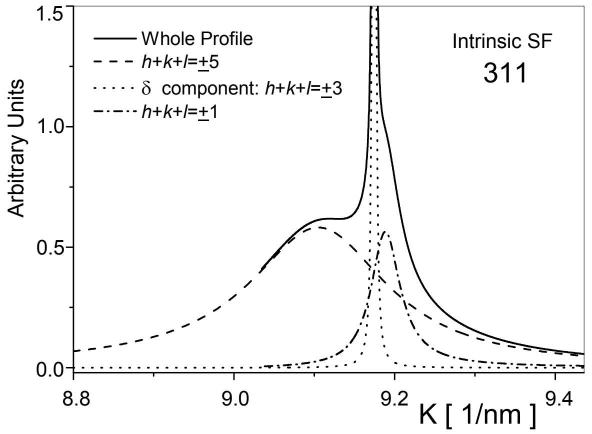

Fig. 6. *The calculated pattern of the {311} Bragg reflection for 4 % intrinsic stacking faults, calculated by the DIFFaX [5] software. The different types of sub-reflections corresponding to the various hkl conditions are also shown. The solid line indicates the whole Bragg reflection which is the sum of the sub-reflections. For the sake of visibility, the unaffected sub-reflection δ is cut off at the relative intensity of 1.5. The angular scale corresponds to copper, which is, however, apart from the scale, the pattern is the same for any other fcc type crystal (by courtesy of Balogh et al. [32]).*

STACKING FAULTS AND TWINNING

In materials with low stacking fault energy faulting and twinning can be one of the major class of lattice defects. In layered or modulated structures faulting and twinning can become so overwhelming that the other two effects, i.e. size and strain, might almost be neglected. This is the case, e.g. in clay minerals. In metals and alloys, especially in hexagonal metals like Ti, Mg and Zr, twinning plays and important role in plastic deformation, since the number of active Burgers vectors is often limited to one or two. On the other hand, in high staking fault energy materials, like Cu or Al for instance, where twinning is not a common mode of deformation, twinning takes over dislocation activity when the grain size is reduced below certain critical values [42, 43]. In the case of hexagonal metals and high staking fault energy nanocrystalline materials stacking faults and twinning occur together with small crystallite size and strain caused by dislocations. In such cases none of the three major lattice defect classes, i.e. size, strain and faulting, can be neglected, they have to be treated simultaneously. As we have seen before, the size and strain effect can be described by uniform size and strain profiles, at least the shape of which are valid throughout the entire diffraction pattern. Both the shape and strain anisotropy can be treated by additional *hkl* dependent scaling factors. In the case of faulting this concept is not straightforward [1, 2, 5, 44, 45], since there is no uniform profile function for the different *hkl* indices. Treacy, Deem and Newsam have developed a computer code, DIFFaX, for calculating the diffraction patterns of faulted or twinned layered structures by using a recursive formalism of scattering [5]. Fig. 6 shows the profile of the 311 Bragg reflection for an *fcc* crystal with 4% intrinsic stacking faults on close packed 111 planes, calculated using the DIFFaX code [32].

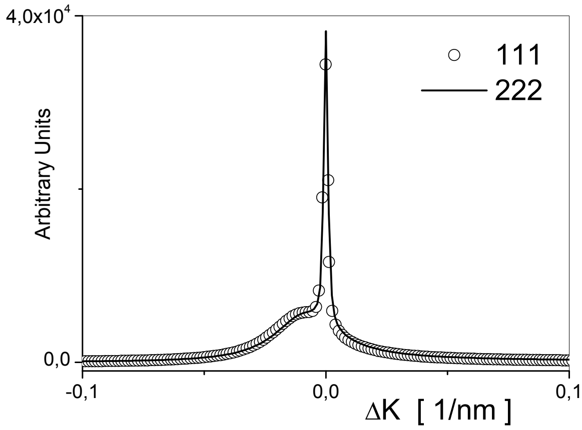

Fig. 7. *The calculated patterns of the {111} (open circles) and {222} (solid line) Bragg reflections for 4 % intrinsic stacking faults, calculated by the DIFFaX [40] software. The profile of the {111} reflection has been mirrored over the exact Bragg position. The angular scale corresponds to copper, however, apart from the scale, the pattern is the same for any other fcc type crystal (by courtesy of Balogh et al. [32]).*

It can be seen that the total profile consists of three sub-profiles which correspond each to a specific *hkl* condition: (i) $h+k+l=\pm 3n$ or (ii) $h+k+l\neq 3n$. In the first case, the profile is unaffected by faulting or twinning; the dotted profile in the figure is the "instrumental" profile in the DIFFaX code. In the second case, the sub-profiles are broadened and shifted to different extent, depending also on *hkl* [32]. The gross features of the *hkl* conditions for the behaviour of the sub-profiles are in good correlation with those described by Warren in [1]. However, the details have not been worked out in [1]. An important aspect of faulting and twinning can be seen in Fig. 7, where the 111 (open circles) and 222 (solid line) profiles corresponding to 4 % intrinsic stacking faults are shown as a function of $\Delta K = (2\cos\theta/\lambda)\Delta\theta$ [32]. Note that ΔK is centred around the exact Bragg position, and the 111 profile has been mirrored over the exact Bragg position. The two profiles are identical, within the slight deviations due to limited accuracy of the numerical calculations. This means that faulting and twinning is *not* a strain, but rather a size-type effect. On the other hand, the two profiles are only identical if one of them is mirrored over the exact Bragg position, i.e. the asymmetry flips over when going from one diffraction order to the next one. This means that it is not a *simple* size-type effect. As it can be seen in Fig. 6, the sub-profiles are shifted and broadened. The shifts are in correlation with the homogeneous deformation caused by planer defects (see also Section "The interference phenomenon in X-ray diffraction from nanocrystalline materials"), whereas the broadening is a consequence of the size-type effect, since faulting and twinning reduces the coherently scattering domain size in the direction perpendicular to the faulted plains.

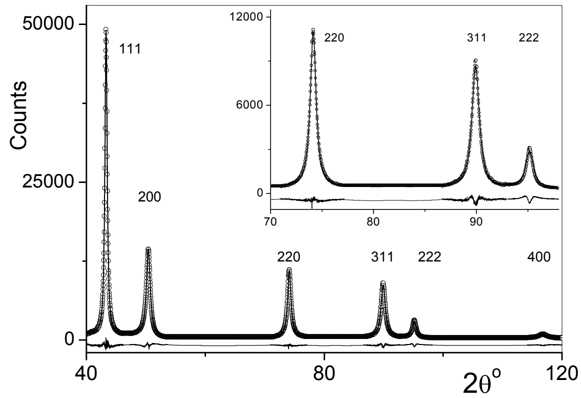

Fig. 8. *Measured (open circles) and fitted (solid lines) diffraction patterns for an inert gas condensed and compacted nanocrystalline copper specimen, cf. [10, 15, 46]. (By courtesy of Balogh et al. [32].)*

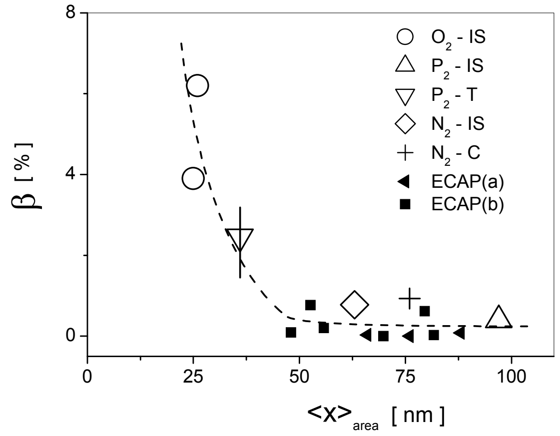

Fig. 9. *The twin density β as a function of the area average mean crystallite or sub-grain size, <x>$_{area}$, for nanocrystalline copper specimens prepared by different methods. For more details see Fig. 9. in [32]. (By courtesy of Balogh et al. [32].)*

Since the sub-profiles are shifted and broadened according to a complex *hkl* algorithm in the different *hkl* reflections, there is no uniform profile function corresponding to planar defects. Nevertheless, in [32] it was realised the individual sub-profiles do behave like uniform profile functions. It was also shown that the sub-profiles are Lorentzian functions over more than 3 orders of magnitude of the intensity distribution, in good correlation with, that faulting and twinning produces size-type line broadening. Some 15.000 sub-profiles were analysed in [32] for broadening and shifting as functions of intrinsic and extrinsic stacking faults, and twin boundaries. As a result, a numerically determined complex *scaling algorithm* was worked out for each class of sub-profiles and each type of planar faults. The *scaling algorithm* is given as a data sheet, also available on the website (http://metal.elte.hu/~levente/stacking), and is built in into the CMWP line profile evaluation code. The extended CMWP code, eCMWP is providing the size distribution, the dislocation structure parameters, and the density of either stacking faults or twin boundaries [32]. The measured (open circles) and fitted (solid lines) diffraction patterns for an inert gas condensed and compacted nanocrystalline copper specimen [10, 46] is shown in Fig. 8.

The best fit was obtained by using the *scaling algorithm* for twins. A large number of nanocrystalline copper specimens, either prepared by large plastic deformation or by inert gas condensation, were evaluated for stacking faults and twins. The result is shown in Fig.9. It can be seen that the twin density β is practically equal to zero when the area average crystallite size is larger than about 40 nm. Below this critical size the twin density increases to relatively high values in good agreement with TEM investigations [43].

REFERENCES

1. B.E. Warren, *Progr. Metal Phys.* **8** (1959) 147.
2. A.J.C. Wilson, *X-Ray Optics, the Diffraction of X-Rays by Finite and Imperfect Crystals*, London, Methuen. 1962.
3. M. Wilkens: *Fundamental Aspects of Dislocation Theory* (Eds. J. A. Simmons, R. de Wit, R. Bullough) Nat. Bur. Stand. Spec. Publ. Vol. II. No. 317. Washington DC, USA, 1970, p. 1195.
4. J.I. Langford, D. Louër, *J. Appl. Cryst.* **24** (1991) 149.
5. M.M.J. Treacy, J.M. Newsam, M.W. Deem, *Proc. Roy. Soc. London* **A433** (1991) 499.
6. M.A. Krivoglaz: *X-ray and Neutron Diffraction in Non-ideal Crystals*, Springer-Verlag, Berlin, Heidelberg, New York, 1996.
7. J.G.M. van Berkum, R. Delhez, Th. H. de Keijser, E.J. Mittemeijer, *Acta Cryst.* **A52** (1996) 730.
8. T. Ungár, A. Borbély, *Appl. Phys. Lett.* **69** (1996) 3173.
9. C.E. Krill, R. Birringer, *Phil. Mag.* **77** (1998) 621.
10. T. Ungár, S. Ott, P. Sanders, A. Borbély, J.R. Weertman, *Acta mater* **46** (1998) 3693.
11. P. Scardi, M. Leoni, *J. Appl. Cryst.* **32** (1999) 671.
12. P.W. Stephens, *J. Appl. Cryst.* **32** (1999) 281.
13. T. Ungár, A. Borbély, G.R. Goren-Muginstein, S. Berger, A.R. Rosen, *Nanostructured Materials* **11** (1999) 103.
14. T. Ungár, G. Tichy, *phys. stat. sol.* **a 147** (1999) 425.
15. T. Mitra, T. Ungár, P.G. Morita, P. Sanders, J.R. Weertman, *Advanced Materials for the 21st Century*, (Eds. Y.W. Chung, D.C. Durand, P.K.

Liaw, G.B. Olson), TMS Warrendale, 1999, p. 553-564.
16. J.I. Langford, D. Louër, P. Scardi, *J. Appl. Cryst.* **33** (2000) 964.
17. T. Ungár, J. Gubicza, G. Ribárik, A. Borbély, *J. Appl. Cryst.* **34** (2001) 298.
18. A.L. Ortiz, F. Sanchez-Bajo, F.L. Cumbrera, F. Guiberteau, *Materials Letters* **49** (2001) 137.
19. P. Scardi, M. Leoni, *Acta Cryst.* **A58** (2002) 190.
20. E. Estevez-Rams, M. Leoni, P. Scardi, B. Aragon-Fernandez, H. Fuess, *Phil. Mag.* **83** (2003) 4045.
21. T. Ida, S. Shimazaki, H. Hibino, H. Toraya, *J. Appl. Cryst.* **36** (2003) 1107.
22. N. Audebrand, S. Raite, D. Louër, *Solid State Sciences* **5** (2003) 783.
23. D. Rafaja, V. Klemm, G. Schreiber, M. Knapp, R. Kužel, *J. Appl. Cryst.* **37** (2004) 613.
24. M. Leoni, P. Scardi, *J. Appl. Cryst.* **37** (2004) 629.
25. G. Ribárik, J. Gubicza, T. Ungár, *Mat. Sci. Eng.* **A387–389** (2004) 343.
26. M. Leoni, A. F. Gualtieri, N. Roveri, *J. Appl. Cryst.* **37** (2004) 166.
27. D. Balzar, N. Audebrand, M.R. Daymond, A. Fitch, A. Hewat, J.I. Langford, A. Le Bail, D. Louër, O. Masson, C.N. McCowan, N.C. Popa, P.W. Stephens, B.H. Toby, *J. Appl. Cryst.* **37** (2004) 911.
28. M. Kasai, E. Matsubara, J. Saida, M. Nakayama, K. Uematsu, T. Zhang, A. Inoue, *Mater. Sci. Eng.* **A 375–377** (2004) 744.
29. T. Ungár, G. Tichy, J. Gubicza, R. J. Hellmig, *Powder Diffraction* **20** (2005) 366.
30. F. Sanchez-Bajo, A. L. Ortiz, F. L. Cumbrera, *J. Appl. Cryst.* **39** (2006) 598.
31. P. Scardi, M. Leoni, *J. Appl. Cryst.* **39** (2006) 24.
32. L. Balogh, G. Ribárik, T. Ungár, *J. Appl. Phys.* **100** (2006) 023512.
33. N. Hansen, X. Huang, W. Pantleon, G. Winther, *Phil. Mag.* **86** (2006) 3981.
34. R. Kužel, *Z. Kristallogr. Suppl.* **23** (2006) 75.
35. J. Gubicza, F. Wéber, *Mater. Sci. Eng.* **A263** (1999) 101.
36. J. Gubicza, J. Szépvölgyi, I. Mohai, L. Zsoldos, T. Ungár, *Mater. Sci. Eng.* **A280** (2000) 263.
37. D. Louër, J.P. Auffrédic, J.I. Langford, D. Ciosmak, J.C. Niepce, *J. Appl. Cryst.* **16** (1983) 183.
38. P. Scardi, M. Leoni, *Acta Cryst.* **A57** (2001), 604.
39. I. Groma, *Phys. Rev.* **B 57** (1998) 7535.
40. G. Ribárik, N. Audebrand, H. Palancher, T. Ungár, D. Louër, *J. Appl. Cryst.* **38** (2005) 912.
41. D. Rafaja, A. Poklad, V. Klemm, G. Schreiber, D. Heger, M. Šíma, M. Dopita, *Thin Solid Films* **514** (2006) 240.
42. M. Chen, E. Ma, K.J. Hemker, H. Sheng, Y. Wang, X. Cheng, *Science* **300** (2003) 1275.
43. X. Z. Liao, Y. H. Zhao, S. G. Srinivasan, Y. T. Zhu, R. Z. Valiev, D. V. Gunderov, *Appl. Phys. Lett.* **84** (2004) 592.
44. E. Estevez-Rams, J. Martinez, A. Penton-Madrigal, R. Lora-Serrano, *Phys. Rev.* **B 63** (2001) 054109.
45. M. Leoni, A. F. Gualtieri, N. Roveric, *J. Appl. Cryst.* **37** (2004) 166.
46. P. G. Sanders, G. E. Fougere, L. J. Thompson, J. A. Eastman, J. R. Weertman, *Nanostruct. Mater.* **8** (1997) 243.

ON STRUCTURAL STUDIES OF SUB-MICROCRYSTALLINE MATERIALS OBTAINED BY SEVERE PLASTIC DEFORMATION – THERMAL STABILITY AND INHOMOGENEITY

R. Kužel[1], V. Cherkaska[1], Z. Matěj[1], J. Čížek[1], J. Pešička[1], M. Masimov[2], R.K. Islamgaliev[3]

[1]Department of Condensed Matter Physics, Faculty of Mathematics and Physics, Charles University, Ke Karlovu 5, 121 16 Praha 2, Czech Republic

[2]Institute of Materials Science, TU Bergakademie Freiberg, Germany

[3]Institute of Physics of Advanced Materials, Ufa State Aviation Technical University, Ufa, Russia

INTRODUCTION

Nanocrystalline materials are single- or multiphase polycrystals with mean grain size below 100 nm. Similar materials with mean grain size of about 100 nm are sometimes also called ultra fine-grained (UFG) or sub-microcrystalline (SMC) materials. They have a number of unusual physical properties induced by significant volume fraction of grain boundaries (GBs) as for example high strength, ductility and high diffusion activity. It is well known that microstructure of UFG materials is determined mainly by the preparation technology. Several techniques of preparation of these materials have been developed so far.

Severe plastic deformation is a technique capable of producing fine-grained sub-microcrystalline (SMC) samples of high purity and no residual porosity [1-4]. In principle, two techniques are used for the strong plastic deformation – equal channel angular pressing (ECAP) and high-pressure torsion (HPT).

Typical feature of NC materials prepared by SPD is non-equilibrium state of GBs with a higher energy and long-range stresses originating from GBs. The crystallographic width of the GBs is narrow, as in usual coarse-grained materials, and it does not exceed 1 nm. The main peculiarity of NC materials prepared by SPD is, however, the presence of an elastically distorted layer near the GBs where the value of the elastic strains is rather high and reaches 3 – 5 %. The thickness of this distorted layer is determined by the degree of the non-equilibrium state of GB structure and is of a few tens of nanometers. The distribution of dislocations is, however, strongly non-uniform: dislocations are arranged along GBs in the distorted layers while the regions inside grains are almost free of dislocations.

EXPERIMENTAL

Different materials mainly deformed by HPT were investigated in our laboratory during last years – semiconductors (silicon, germanium), fcc metals (copper, nickel, copper with different amount of Al_2O_3), bcc metals (iron), hexagonal metals (magnesium, magnesium with addition of gadolinium) – by different techniques: X-ray diffraction (XRD), life-time positron spectroscopy (PL), transmission electron microscopy (TEM), differential scanning calorimetry (DSC), microhardness measurements. The evolution of microstructure with the temperature and phase composition of the materials was studied. Characteristic grain growth with annealing temperature was investigated also by X-ray Debye patterns recorded in the back-scattering modus and by the EBSD technique. In addition, a new method for crystallite size estimation – diffuse scattering in the transmitted wave – was tested for the copper samples.

Samples were subjected to severe plastic deformation by high pressure torsion (3 – 6 GPa). The thin foil disc samples were prepared in Ufa Aviation Technical University, Russia (diameter of about 1 cm for Cu and less down to 1 mm for Ge and Si).

XRD measurements were carried out with the aid of the XRD7 (Seifert-FPM) and HZG4 powder diffractometers using filtered CuK_α and MoK_α radiation, respectively. XRD profiles were fitted with the Pearson VII function by the program DIFPATAN [5]. The lattice parameters were determined by the Cohen-Wagner extrapolation plot (a_{hkl} vs. cos θ cot θ), preferred grain orientation was characterized by the Harris texture indices. XRD line broadening was evaluated simply by integral breadths (β) and FWHMs. The correction for instrumental broadening was performed with the aid of NIST LaB_6 standard and the Voigt function method. Then the modified Williamson-Hall (WH) plots (β vs. sin θ) were used for the evaluation [6, 7]. For selected samples also total pattern fitting was applied.

PHASE ANALYSIS, LATTICE PARAMETERS, TEXTURES

Additional phases appeared after deformation in germanium and silicon samples and minor phases were detected in Mg-Gd samples during annealing.

The analysis of as-deformed samples has shown the presence of two Ge phases – the most common cubic phase with the space group $Fd\bar{3}m$ and high-pressure tetragonal phase with the space group $P4_32_12$. The measured lattice parameters (a = 5.960(3) Å, c = 6.988(7) Å) agrees quite well with the tabulated values [8]. The content of 8 wt% of the phase was estimated. With increasing annealing temperature the line widths of cubic phase and content of tetragonal phase decrease (Fig. 1). The phase completely disappeared after annealing at 400 ºC. High-pressure phase was also detected in silicon samples (cubic – $Ia3$) [9, 10].

Lattice parameters of all the samples under study agreed well with the tabulated values that indicates absence of significant stresses. Preferred grain orientation was negligible for iron and not too strong for copper samples when often mixed two component texture <111> - < 100> was found. More pronounced texture was detected in magnesium samples (000l).

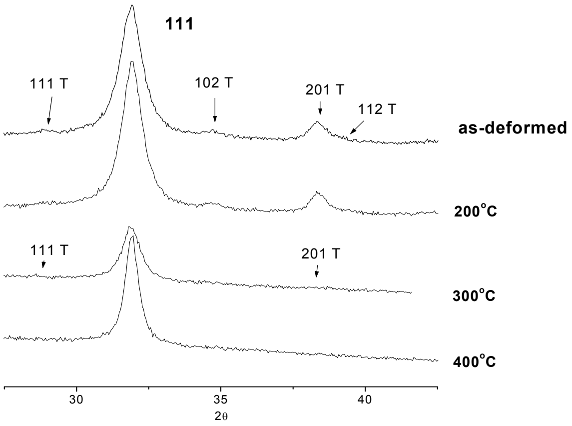

Fig. 1. *Evolution of the XRD powder patterns of deformed Ge sample with annealing temperature. High-pressure tetragonal phase (T) completely disappeared after annealing at 400 C.*

SIMPLIFIED LINE PROFILE ANALYSIS

Williamson-Hall plots can well be used for visualization of basic features of line broadening – finding main source of broadening, line broadening anisotropy, basic trends in series of samples. However, one must be very careful with the quantitative evaluation unless either size or strain effect is clearly dominating. For most of the as-deformed samples this was the strain broadening. Then the following formula can be used for the dislocation density estimation

$$\beta_h = b\sqrt{\rho}\sqrt{\chi_h}\sqrt{2\ln P}\,A\frac{\sin\theta}{\lambda}, \qquad (1)$$

β is the integral breadth (in the units of the reciprocal space, 1/d), ρ is the mean dislocation density, b is the magnitude of the Burgers vector, the P factor is related to the correlation in dislocation arrangement and factor A is close to unity.

For dislocation density determination, the knowledge of the orientation factor χ_h (often called as contrast factor and denoted by C) is necessary. The correlation factor P must be estimated for example from the profile shape or better from the Fourier coefficients. Of course, this is the main source of uncertainty in this procedure.

The orientation factor depends on the indices h, k, l and determines the anisotropy of line broadening. General relations for calculation of the orientation factors were derived in papers [11, 12]. In order to calculate the factor, some model – dislocation types must be considered. Crystal symmetry must also be taken into account and corresponding averaging over all symmetrically equivalent directions must be performed for the calculations of orientation factors. In case of preferred orientation of lattice defects in the sample, which may be related to the preferred grain orientation in some way, appropriate weights must be taken in the averaging. Useful simple relations for orientation factors of polycrystalline cubic and hexagonal materials without preferred grain and defect orientation were derived by Ungar et al [13-15]. The relations are based on invariants typical for different symmetries. For cubic materials it is

$$\langle \chi_{hkl} \rangle = \langle \chi_{hkl} \rangle (1+qH)\cdot \left[1+q\frac{h^2k^2+k^2l^2+l^2h^2}{(h^2+k^2+l^2)}\right] \qquad (3)$$

If the elastic constants of the material are known, two parameters $\langle \chi_{h00} \rangle$ a q can be expressed as functions of elastic constants and then easily calculated for different dislocation types [14]. Recently, the program ANIZC has been made available. This can calculate orientation factors for cubic, hexagonal and trigonal crystals [16].

It should be emphasized that it is this factor which can make possible to estimate not only dislocation density but also the dislocation content. In most cases, these factors could account well for the observed line broadening anisotropy as it is shown on Fig. 2 for different HPT deformed materials. The orientation factors were calculated for the most common dislocations in fcc lattice (for copper, nickel) and diamond structure type (germanium), i.e. edge and screw dislocations with the Burgers vector ***b*** || <110>, and for the bcc lattice the dislocations with the Burgers vector ***b*** || <111>.

TOTAL PATTERN FITTING

In order to avoid rough and often inappropriate simplification of the above method, more sophisticated methods should be used. Traditional Fourier analysis is being replaced by the multiple peaks or whole pattern fitting. The procedure also include convolution with instrumental profile. Originally, the idea of simultaneous fitting of more orders of reflections for size-strain analysis was introduced by Houska et al [17, 18], extended for stacking faults [19] and applied also to analysis of HPT deformed germanium. Nowadays, two program systems for this approach based on the description by realistic microstructural model are being developed in groups of Paolo Scardi (e.g. [20], [21]) and Tamas Ungar [22]. Both are successfully using explicit formulae for the description of both dislocation-induced line and size broadening and have been applied to different kind of materials. Essentially four free parameters are used – dislocation density, dislocation correlation factor, mean crystallite size and variance of the size distribution. Even though, the description is more physically realistic than approximate methods based on integral breadth, the fitting must be used with a caution and the fitting cannot be done in a fully automatic mode. General problem is a high correlation between the dislocation density and dislocation correlation parameter and also the two size parameters. The correlation is intrinsic in the description and cannot be completely overcome by using different optimization procedures. In any case, high-quality data are required for successful fitting. Example of fitting for the Ge sample annealed at 400 ºC is shown in Fig. 3.

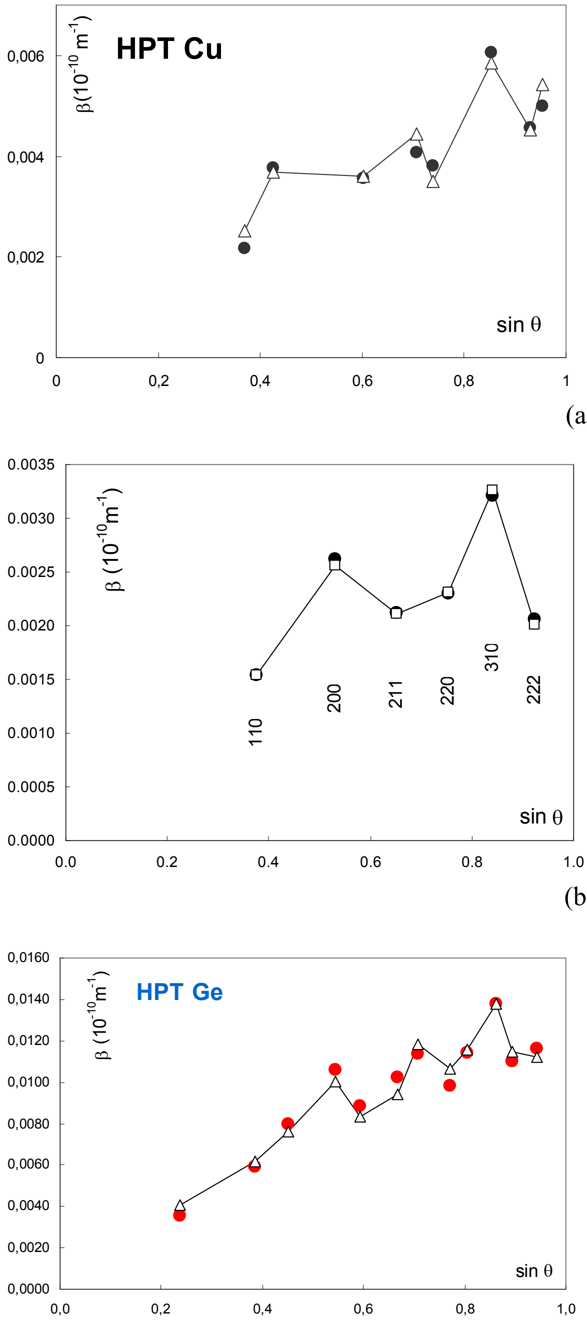

(a)

(b)

(c)

Fig. 2. *Typical Williamson-Hall plots for high-pressure torsion deformed Cu (a), Fe (b) and Ge (c).Full symbols represent experimental data, open symbols (connected by line) correspond to the calculated values.*

MICROSTRUCTURE OF HPT DEFORMED SAMPLES

In general, the microstructure of Ge and Si samples show significantly smaller crystallites of about 10 nm and dislocation densities of 5 × 10^{15} m^{-2}. Crystallite size of metals (Cu, Ni and Fe) is one order of magnitude larger having a wide distribution and maximum values in the range 100 – 200 nm. Dislocation densities are lower than 1 × 10^{15} m^{-2}, usually 6 – 7 × 10^{14} m^{-2}.

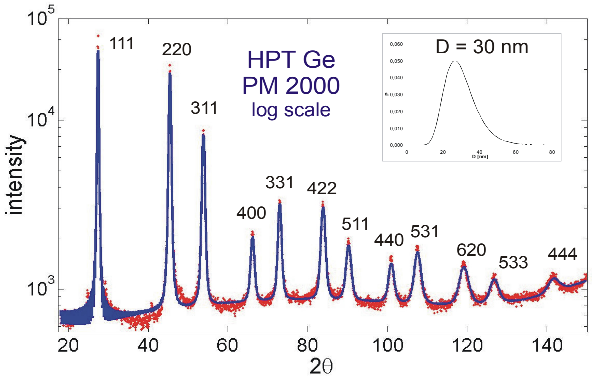

Fig. 3. *Total pattern fitting for partially annealed (400 °C) Ge sample (fitted by the program pm2k).*

TEM micrographs (Fig. 4) show highly defected structure with inhomogeneous distribution of defects (regions with high and low dislocation density). Dislocations are situated in distorted regions along GBs, while grain interiors are almost free of dislocations, for detailed discussion see [23]. On the other hand, UFG Mg and UFG Mg-10 wt. % Gd exhibit homogeneous distribution of dislocations throughout whole grain.

Obtained values of the dislocation density agree quite well with the estimations made from TEM for as-deformed samples (Fig. 4a). The crystallite size distributions obtained from both methods are not identical but not much different either. It must be taken into account that the XRD is sensitive to coherent domain size and in the case of TEM of strongly deformed materials it is often rather difficult to define grains on the pictures.

Positron life-time spectra show usually three major components – component with lifetime well below 100 ps can be obviously attributed to free positrons. Relative intensity of this component is very small for most of the as-deformed samples. It clearly indicates that majority of positrons annihilate from trapped states at defects. The second component is dominating and comes from positrons trapped at dislocations. For example, the lifetime of this component for UFG Cu and UFG Cu with Al_2O_3 corresponds to the lifetime 164 ps of positrons trapped at Cu dislocations [23, 24]. The third component with the longest lifetime represents a contribution of positrons trapped at micro-voids inside grains [23]. Using theoretical calculations in Ref. [23], one obtains that size of the micro-voids in the as-deformed UFG Cu specimen corresponds to 5 mono-vacancies. Larger micro-voids (more than 10 vacancies) were found in UFG Fe. On the other hand, no micro-voids were detected in UFG Mg and UFG Mg-10 wt% Gd.

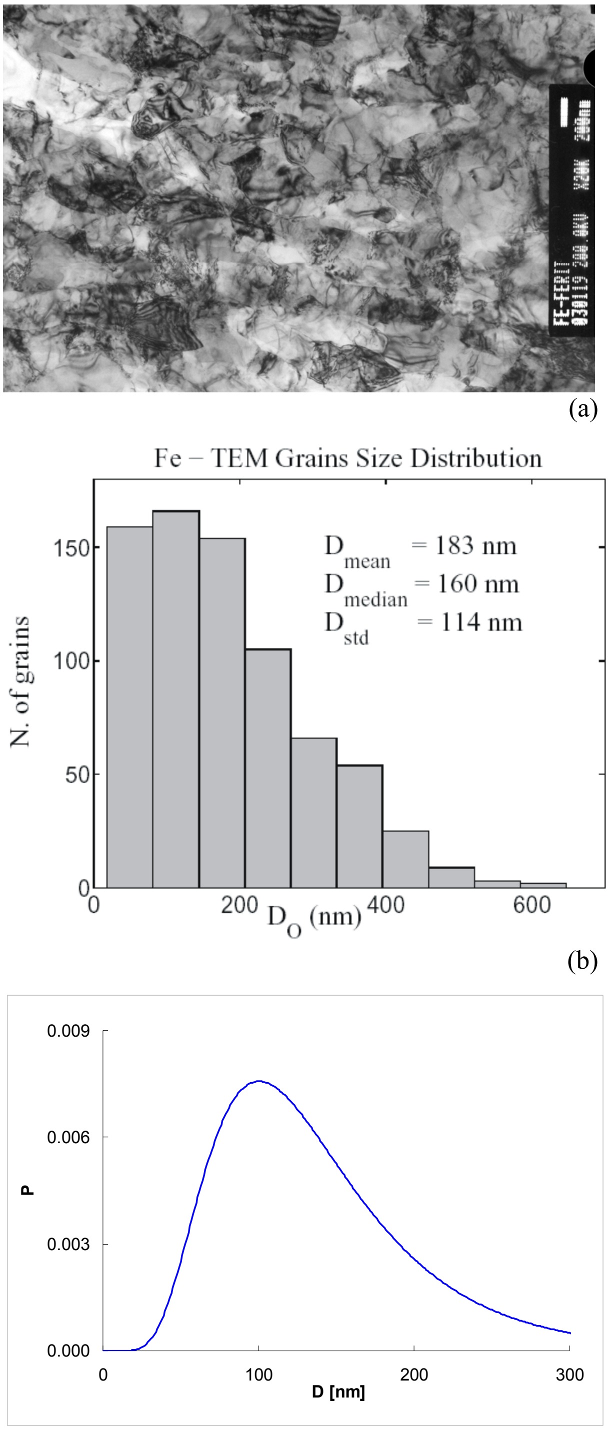

Fig. 4. *Typical TEM micrographs of as-deformed iron (a - marked scale – 200 nm), corresponding histogram of estimated grain size distribution (b) and log-normal size distribution corresponding to the parameters obtained from the total pattern fitting by the program pm2k.*

THERMAL STABILITY OF THE MICROSTRUCTURE

Some results of our studies have been published, e.g. in [6, 25-27]. Thermal stability of the fine highly defected microstructure is not very high for pure metals. Usually strain recovery is followed by the grain growth. For copper samples, significant drop of line broadening is observed already after annealing at 150-200 ºC. It was found that the addition of at least 0.5 wt. % Al_2O_3 prevents grain growth and keeps the dislocation density high and crystallites small up to about 400°C. The amount of 0.3 wt. % is insufficient for that and a rapid grain growth is observed at about 200°C. Higher amount 1.1 wt. % Al_2O_3 does not improve stability considerably.

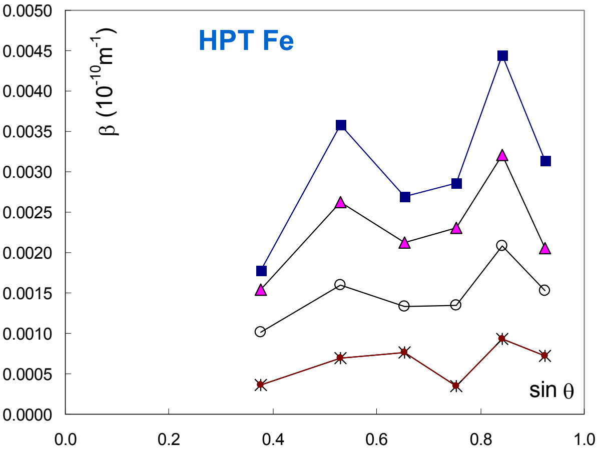

Fig. 5. *Evolution of the Williamson-Hall plot with annealing temperature (from the top – as-deformed, 130ºC, 190ºC, 370ºC). All points correspond to the experimental values after correction on instrumental broadening.*

For iron samples, continuous strain recovery is observed in the range 130-200°C (Fig. 5). However, microstructural changes at about 200 ºC are accompanied by an increase of line broadening and decrease of WH plot slope. Magnesium samples did not show significant line broadening even after severe deformation at room temperature. Addition of 10 % of Gd leads to finer and highly defected microstructure which remains stable up to about 220 ºC. A decrease of defect density and grain growth with increasing temperature during isochronal annealing lead to rise of the intensity of the free positron component in PL spectra accompanied by a decrease of the intensities of positrons trapped at defects [28]. A typical example of temperature dependence of the relative intensities of positron components is plotted in Fig. 6 for UFG Cu.

INHOMOGENEITY

In-plane inhomogeneity for as-deformed disc samples was found by positron annihilation [29, 30] but not by XRD. The diameter of the analyzed region was similar in both cases (4 mm). Therefore, it was explained by the inhomogeneous distribution of micro-voids.

In-depth gradients were found by both techniques. In Fig. 7, the WH plots are shown constructed for as-deformed copper and for high-resolution parallel beam measurements with rotating anode, Goebel mirror in the incident beam and two crystals in the diffracted beam – quartz (101) and graphite (001). While there is no difference between centre and margin of the specimen, clear difference can be seen for plots obtained in symmetrical scan and the one at the fixed angle of incidence γ = 5 °. In the latter case, the penetration depth is smaller, which means a higher defect density on the surface. Therefore, in order to remove the surface layer, the samples were etched before most of XRD measurements.

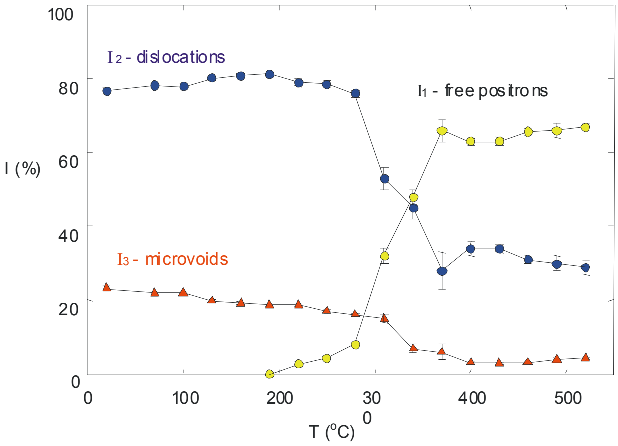

Fig. 6. *Temperature dependence of relative intensities of positron component resolved in positron lifetime spectrum of UFG Cu prepared by high pressure torsion using pressure p = 3 GPa.*

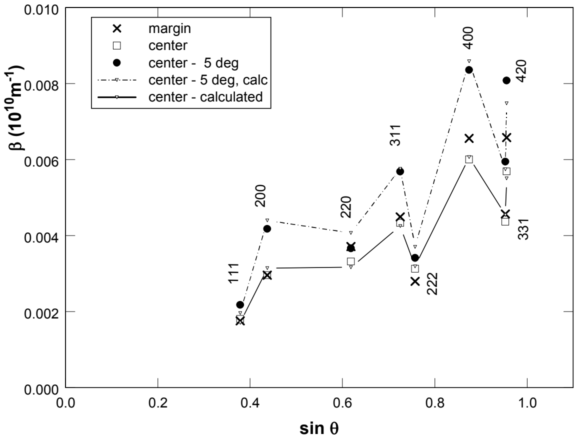

Fig. 7. *Williamson-Hall plots for Cu + 0.5 % Al_2O_3 sample measured in the centre (□), at the margin (x) and in the centre by 2θ scan at low angle of incidence (●).*

A different picture appeared after annealing. Valuable results were obtained by the classical simple back-reflection method. For as-prepared samples, continuous Debye rings were observed while after annealing a few dots were clearly distinguished on them indicating fast growth of only a few grains. This appeared at lower temperatures, before any significant changes of line broadening and PL spectra and it was only detected for copper samples while for iron and magnesium the grain growth seems to be homogeneous.

In-plane inhomogeneity was also detected by the back-reflection. In the margin regions of disc specimens, larger grains were detected than in their centers. The effect appeared only after annealing above

200 °C, not in the as-prepared state and only for copper samples.

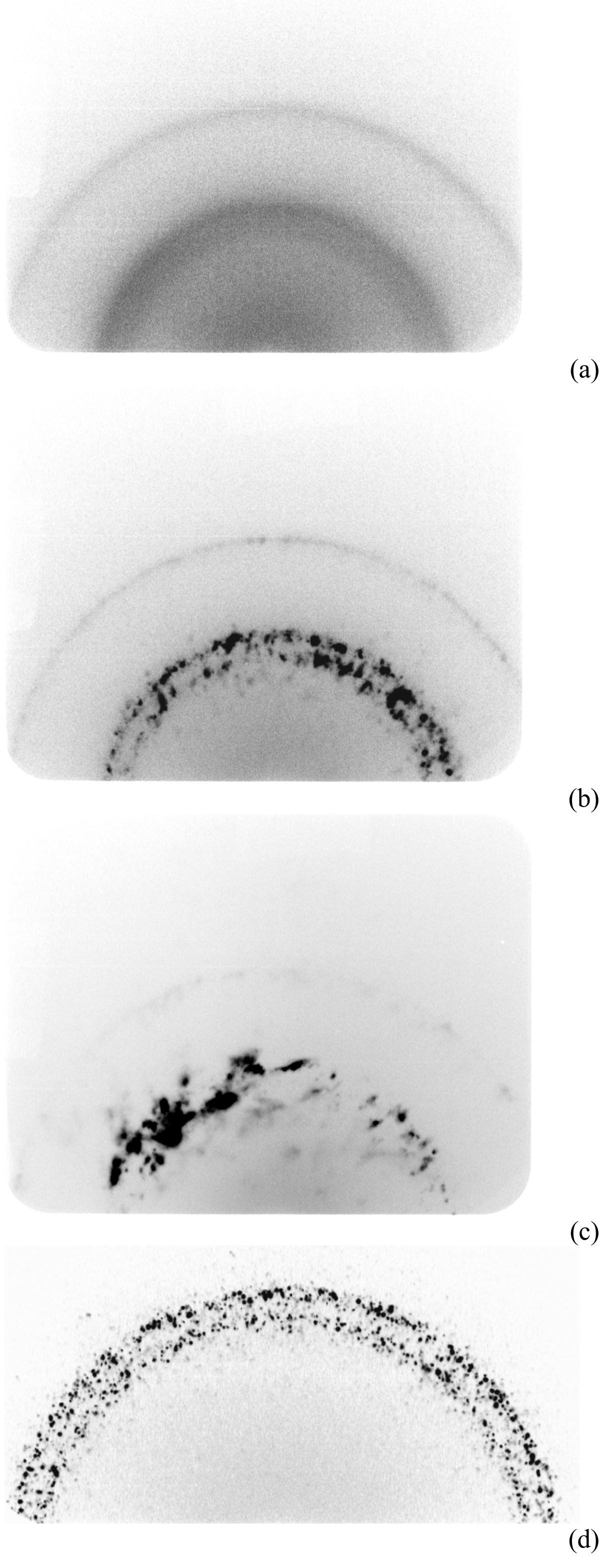

Fig. 8. *Fragments of the Debye rings obtained by back-reflection for as-deformed sample Cu + 0.5 % Al_2O_3 (a), the center of the same sample after annealing at 550 °C (b), margin of the sample after annealing at 550 °C (c), Fe sample after annealing at 550 °C.*

In Fig. 8, four cases are compared – rings for as-deformed state (a), for the central region of annealed sample (b), for outer region of the disc of the same sample (c) and for annealed iron sample (d). Strong inhomogeneity can be observed especially for copper while for iron the distribution of dots and consequently also grains is quite homogeneous. With increasing annealing temperature such effects can be seen on diffraction profiles as well. This also makes conventional way of powder XRD line profile analysis impossible.

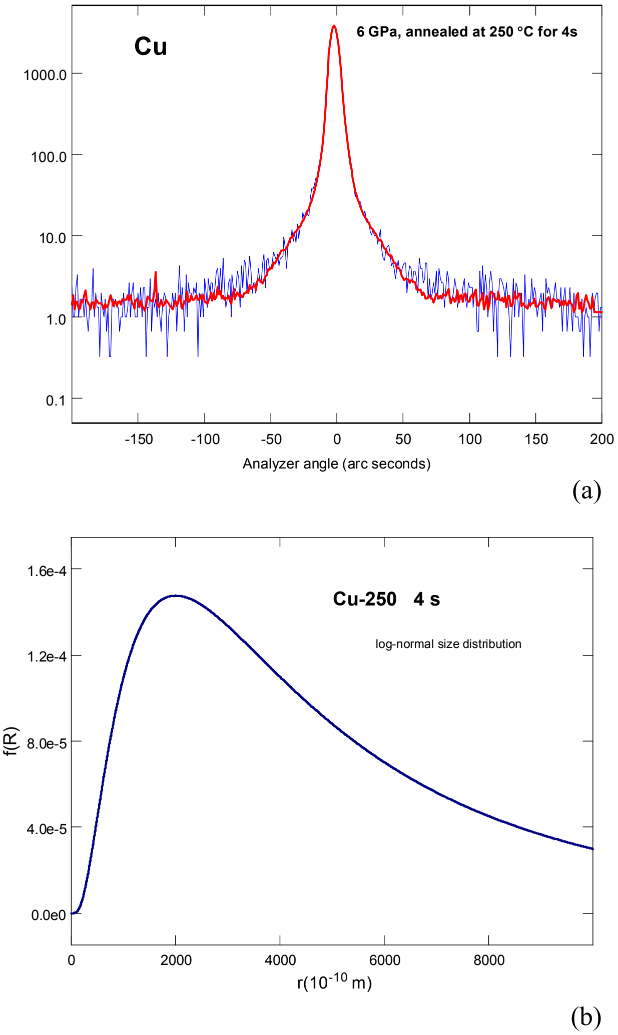

Fig. 9. *Experimental profile of the transmitted wave including diffuse scattering (thin line) and corresponding theoretical curve (fit, thick line) for the deformed copper annealed at 250 ºC (a), log-normal size distribution used for the calculation of theoretical curve.*

A new method of measurements of the diffuse scattering by small crystallite size in the transmitted wave has been applied [31]. It consists in the comparison of intensity profiles with and without diffuse scattering. It requires compact specimen with an appropriate thickness. It should be thick enough in order to measure the diffuse scattering but sufficiently thin in order to measure the transmitted intensity. For copper this means the sample thickness of about 0.1 mm. After careful alignment of the equipment with several crystal monochromators (to cut the tails of instrumental profile), measurements are very simple and fast. There was a hope to separate independently size and strain effect by this method and line profile analysis. However, in the case of strong deformation, the effect is smeared out and therefore none of this type diffuse scattering was measured. By contrast, it was well detected on the copper samples annealed at 250 °C. In Fig 9a, the intensity profile of the transmitted wave is shown in log scale together with a fit [31]. For successful fit it was necessary either to use a model of bimodal size distribution or a very broad log-normal size distribution (Fig. 9b). This is in agreement both with the back-reflection method an also the EBSD. The map obtained by the EBSD is shown in Fig. 10.

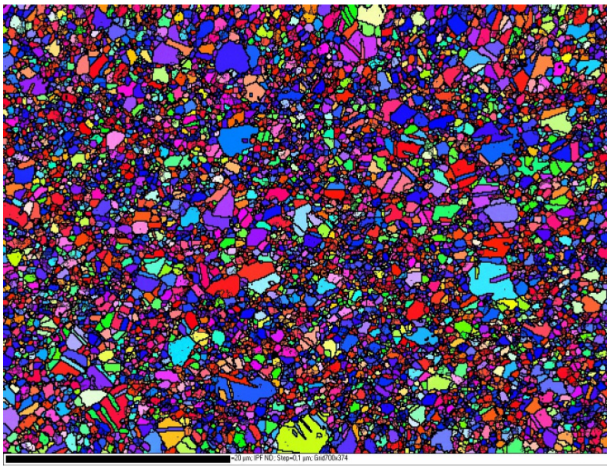

Fig. 10. *EBSD map of the deformed copper annealed at 250 °C for 4 s. The bottom black marker corresponds to 20 µm.*

CONCLUSIONS

Possibilities of the X-ray powder diffraction – phase analysis, lattice parameter determination, texture, stresses and line profile analysis – can well be used for investigations of sub-microcrystalline materials obtained by severe plastic deformation. They can be combined with other X-ray techniques, both old and new (2D picture of the Debye rings, diffuse scattering in the transmitted wave), as it was shown in the article. Of course, they should always be complemented with other techniques like for example TEM giving qualitative and local direct pictures of the microstructure, EBSD showing orientation and crystallite size maps, positron annihilation spectroscopy, which could be sensitive to specific lattice defects like micro-voids. Of course, other methods like microhardness and resistivity measurements can be very useful for obtaining overall microstructural picture.

In case of XRD technique, there are still challenging problems to be solved, for example, an appropriate theoretical description of the scattering by strongly inhomogeneous distribution of dislocations, influence and separation of the 2nd kind stresses or the role and description of disclinations.

ACKNOWLEDGEMENTS

This work is a part of the research program MSM 0021620834 financed by the Ministry of Education of the Czech Republic.

REFERENCES

[1] R. Z. Valiev, *Mat. Sci. Eng.* **A234-236** (1997) 59.
[2] R. Z. Valiev, *Nanostructured Mater.* **6** (1995) 173.
[3] R. Z. Valiev, I. V. Alexandrov, R. K. Islamgaliev: *Nanostructured Materials Sci. Technol.*, ed. Chow G. M., Noskova N. I. – NATO ASI: Kluwer Publication. 1998, p. 121-143.
[4] R. Z. Valiev, R. K. Islamgaliev, I. V. Alexandrov, *Prog. Mater. Sci.* **45** (2000) 103.
[5] DIFPATAN – program for powder pattern analysis. R. Kužel, http://www.xray.cz/priv/kuzel/difpatan.
[6] R. Kužel, J. Čížek, I. Procházka, F. Chmelík, R. K. Islamgaliev, N. M. Amirkhanov, *Mat. Sci. Forum* **378-381** (2001) 463.
[7] R. Kužel, Jr., R. Černý, V. Valvoda, M. Blomberg, and M. Merisalo, *Thin Solid Films* **247** (1994) 64.
[8] PDF2 or PDF4 database, www.icdd.com.
[9] R.K. Islamgaliev, R. Kužel, E.D. Obraztsova, J. Burianek, F. Chmelik, R. Z. Valiev, *Mat. Sci. Eng.* **A 249** (1998) 152.
[10] R.K. Islamgaliev, R. Kužel, S.N. Mikov, A.V. Igo, J. Buriánek, F. Chmelík, R.Z. Valiev, *Mat. Sci. Eng.* **A 266** (1999) 205.
[11] P. Klimanek, R. Kužel, Jr., *J. Appl. Cryst.* **21** (1988) 59.
[12] R. Kužel, Jr., P. Klimanek, *J. Appl. Cryst.* **21** (1988) 363.
[13] T. Ungár, G. Tichý, *phys. stat. sol.* **17** (1999) 42.
[14] T. Ungár, I. Dragomir, A. Révész, A. Borbély, *J. Appl. Cryst.* **32** (1999) 992.
[15] I. Dragomir, T. Ungár, *J. Appl. Cryst.* **35** (2002) 556.
[16] A. Borbély, J. Dragomir-Cernatescu, G. Ribárik, T. Ungár, *J. Appl. Cryst.* **36** (2003) 160.
[17] T. Adler, C. R. Houska, *J. Appl. Phys.* **17** (1979) 3282.
[18] C. R. Houska, T. M. Smith, *J. Appl. Phys.* **52** (1981) 748.
[19] C.R. Houska, R. Kuzel, in *Defect and Microstructure Analysis by Diffraction.* Ed. by R. L. Snyder, J. Fiala and H. J. Bunge, Oxford University Press, 1999, pp. 141-164.
[20] P. Scardi, M. Leoni, *Acta Cryst.* **A58** (2002) 190.
[21] P. Scardi, M. Leoni, Y. H. Dong, *Eur. Phys. J.* **B18** (2000) 23.
[22] T. Ungár, J. Gubicza, G. Ribárik, A. J. Borbély, *J. Appl. Cryst.* **34** (2001) 298.
[23] J. Čížek, I. Procházka, M. Cieslar, R. Kužel, J. Kuriplach, F. Chmelík, I. Stulíková, F. Bečvář, R.K. Islamgaliev, *Phys. Rev.* **B65** (2002) 094106.
[24] J. Čížek, I. Procházka, P. Vostrý, F. Chmelík, R.K. Islamgaliev, *Acta Phys. Polonica* **A95** (1999) 487.
[25] R. Kužel, Z. Matěj, V. Cherkaska, J. Pešička, J.

Čížek, I. Procházka, R. K. Islamgaliev, *J. Alloys Comp.* **378** (2004) 242.

[26] J. Čížek, I. Procházka, B. Smola, I. Stulíková, R. Kužel, Z. Matěj, V. Cherkaska, R.K. Islamgaliev, O. Kulyasova, *Acta Phys. Polonica* **107** (2004) 738.

[27] J. Čížek, I. Procházka, B. Smola, I. Stulíková, R. Kužel, Z. Matěj, V. Cherkaska, R.K. Islamgaliev, O. Kulyasova, *Mat. Sci. Forum* **482** (2005) 183.

[28] J. Čížek, I. Procházka, R. Kužel, M. Cieslar, R.K. Islamgaliev, *J. Metastable Nanocrystalline Materials* **17** (2003) 37.

[29] J. Čížek, I. Procházka, G. Brauer, W. Anwand, R. Kužel, M. Cieslar, R. K. Islamgaliev, *J. Metastable Nanocrystalline Materials* **17** (2003) 23.

[30] J. Čížek, I. Procházka, G. Brauer, W. Anwand, R. Kužel, M. Cieslar, R. K. Islamgaliev, *phys. stat. sol.* **a 195** (2003) 335.

[31] R. Kužel, V. Holý, M. Čerňanský, J. Kuběna, D. Šimek, J. Kub, in "*Diffraction Analysis of the Microstructure of Materials*". Ed. P. Scardi, E. J. Mittemeijer. Springer Series in Materials Science 68. 2003. Springer. Berlin. Heidelberg. 229.

NEW HIGH-TEMPERATURE FURNACE FOR SANS MEASUREMENTS AT DN-2 DOUBLE-BENT-CRYSTAL DIFFRACTOMETER IN NPI ŘEŽ NEAR PRAGUE

P. Strunz[1], J. Šaroun[2], P. Lukáš[1], P. Mikula[2], J. Zrník[3]

[1]Nuclear Physics Institute (NPI), CZ-25068 Řež near Prague, Czech Republic

[2]Research Centre Řež, CZ-25068 Řež near Prague, Czech Republic

[3]Technical University of Košice, Dept. of Materials Science, Park Komenského 11, 04001 Košice, Slovakia

INTRODUCTION

One of the advantages of the neutron radiation is usually a weak absorption by matter (and thus also by sample environment windows). It enables relatively easy investigations at extreme conditions, e.g. at high temperatures, in the bulk of various materials. For example, super-alloys (single-crystalline and polycrystalline) and ceramics are both processed and used at high temperatures, which brings two strong reasons to investigate their microstructure in-situ in the temperature region that is not easily accessible by other techniques. Small-Angle Neutron Scattering (SANS) can detect evolution of precipitates and pores in these materials. There is a number of in-situ SANS studies at high temperatures using conventional pin-hole SANS machines for microstructural characterization of these solids on nano-scale (e.g. [1] – [4] and references therein) using standard furnaces for neutron scattering. However, a complementary double-bent-crystal SANS technique [5] was not yet – to the authors knowledge – used for material characterization at very high temperatures (i.e. over 1000°C), although its use would be desirable in many cases. For example, nickel-base super-alloys are strengthened by precipitates, size of which ranges from tens of nanometres to 1 μm and complementary studies of precipitate dissolution and formation would help to optimize the heat treatment of the super-alloys.

Therefore, a high-temperature furnace implementation project was realized at DN-2 facility of Neutron Physics Laboratory (NPL), NPI Řež near Prague (Czech Republic) in 2006 which fits into the frame of one topic (microstructure characterization of alloys and ceramics) investigated at NPL.

SANS FACILITY DN-2

DN-2 is a double-bent-crystal diffractometer dedicated to high-resolution SANS measurements ([6], [7]) that is located at the research reactor LVR-15. It employs neutron diffraction optics (bent silicon crystals) in order to transform the angular deviation into the spatial one, which enables the use of a linear position-sensitive detector for faster data collection. DN-2 device belongs to the NPL facilities, which are also accessible for external users [8]. Groups coming from the EU Member Countries and Associated Countries may qualify for a travel grant provided by the European Commission under NMI3 project (FP6: RII3-CT-2003-505925).

With respect to the pin-hole SANS facilities, DN-2 can achieve lower magnitudes of scattering vector Q ($Q=|\mathbf{Q}|=4\pi\sin\theta/\lambda$, 2θ is the full scattering angle, λ is the neutron wavelength). The minimum Q is $1.5\times10^{-4}\,\text{Å}^{-1}$, significantly lower than the minimum ($5\times10^{-4}\,\text{Å}^{-1}$) at the well-known pin-hole facility D11 in ILL Grenoble. At the same time, a lower neutron wavelength λ is used (2.09 Å) which very significantly reduces multiple scattering effects. Due to the possibility of bending of monochromator and analyzer crystals, a Q-range most suitable for the particular experiment can be tuned.

HIGH-TEMPERATURE FURNACE

The radiation furnace (3016VAK) for DN-2 was constructed by CLASIC Řevnice and tested in summer 2006. The furnace placed at sample position at DN-2 is shown in Fig. 1.

The sample space (height 60 mm, diameter 30 mm) in the radiation furnace is heated by four Super-Kanthal elements. The furnace can be cooled by water flowing through the double coat (Julabo cooler, closed circuit). In order to fulfil geometrical requirements of double-bent-crystal arrangement, the outer diameter of the furnace was suppressed down to 160 mm. The parameters of the furnace are the following:

- medium: vacuum, air, inert gas
- maximum temperature for long-term treatment 1450°
- maximum peak temperature 1500°C
- temperature detection: thermocouple W-Re.
- regulation: CLARE 4.0
- window: 4x (90° angular spacing), quartz or Al

As the furnace is dedicated to the double-bent-crystal SANS (it implies very small scattering angles), only narrow openings for the incoming and outgoing beam are needed. Therefore, no thermal shielding is in the direction of openings and only quartz glass windows are in the beam. In this way, relatively low scattering background is achieved, moreover independent on the temperature.

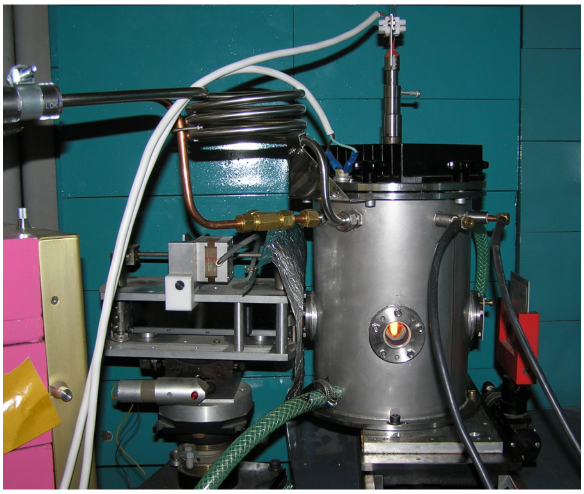

Fig. 1. *A high-temperature measurement at DN-2.*

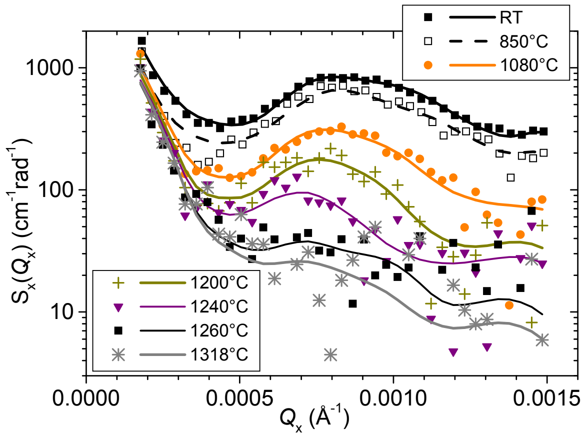

Fig. 2. *The measured and fitted scattering curves* $S_x(Q_x)$ *for CMSX4 sample during increasing temperature. For double-crystal arrangement,* $S_x(Q_x)$ *corresponds to the differential macroscopic cross section* $d\Sigma/d\Omega(Q_x,Q_y)$ *integrated over the vertical angular component.*

DISSOLUTION OF PRECIPITATES IN CMSX4

As an example of experiment using the furnace, a testing measurement with CMSX4 commercial super-alloy is presented here. In this super-alloy, a dense system of γ' precipitates is the main strengthening factor and their microstructure plays an essential role in the mechanical properties. The morphology is controlled by the heat treatment, the first part of which causes dissolution of the precipitates formed during casting. The dissolution is accompanied by the homogenization of the chemical composition throughout the alloy. For an optimum homogenization, the temperature must be high enough to take into solution even the coarse inter-dendritic precipitates, but sufficiently low to avoid incipient melting.

In Fig. 2, a series of selected scattering curves taken during the temperature increase shows evolution of γ'-precipitate microstructure at different temperatures. The visible inter-particle interference peak determines the distance between the precipitates in the dense packed precipitate system. The model of the microstructure used in the fit to the measured data is displayed in Fig. 3. Program NOC [9] which was used for the evaluation employs this 3D model.

Fig. 4 displays parameters obtained from the evaluation. Although the effects of the volume fraction and the change of the scattering contrast cannot be separated easily (as the dissolution of smaller precipitates changes the composition of the γ matrix and thus also the scattering contrast of the larger precipitates), a significant volume fraction decrease can be deduced above 1000°C. Practically all ordered γ' precipitates dissolve fully between 1240 and 1260°C (the inter-particle interference maximum disappears – see Fig. 2). Above this temperature, only larger inhomogeneities remain in the sample (see the scattering curve in Fig. 2 at very low *Q*-values).

On the other hand, the distance between the precipitates (see Fig. 4) remains nearly unchanged up to 1200°C. It indicates, that the dissolution occurs inhomogeneously, i.e. that there is still ordered precipi-

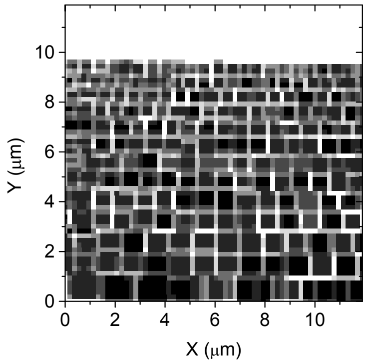

Fig. 3. *The section through 3D model of ordered γ' precipitates used for the SANS data evaluation of CMSX4 in-situ measurement.*

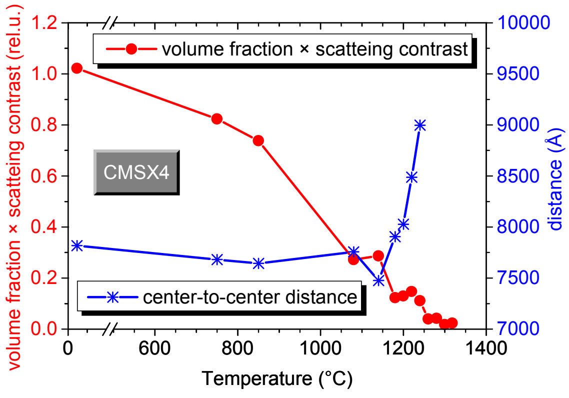

Fig. 4. *The evolution of the volume fraction times scattering contrast and mean distance of the ordered γ' precipitates.*

tate microstructure at some places in the sample while the precipitates are completely dissolved in the other parts.

CONCLUSIONS

The first tests confirmed the applicability of the new equipment for in-situ SANS studies at elevated temperatures. Among many prospective fields of the use of high-temperature furnace at high-resolution SANS instrument belong:

- Slow kinetics studies of microstructure of high-temperature materials
- Morphological transformations dependent on temperature change
- Phase transformations
- Formation/dissolution of precipitates in alloys
- Mesoscopic porosity in ceramics, metals and other materials
- Sintering
- Study of non-magnetic part of scattering over Curie temperature.

DN-2 SANS machine equipped with the furnace is open (on proposal basis) to the external users.

ACKNOWLEDGEMENTS

The project was supported by IRP AV0Z10480505 and the grant MSM 2672244501. The authors are indebted to the company CLASIC CZ, for a fruitful cooperation on the furnace prototype.

REFERENCES

[1] D. del Genovese, P. Strunz, D. Mukherji, R. Gilles, J. Rösler, *Metal. Mater. Trans.* **A36** (2005) 3439-3450.
[2] P. Strunz, G. Schumacher, R. Vaßen, A. Wiedenmann, V. Ryukhtin, *Scripta Mater.* **55** (2006) 545-548.
[3] P. Strunz, D. Mukherji, R. Gilles, J. Rösler, A. Wiedenmann, *Mat. Sci. Forum* **426-432** (2003) 821-826.
[4] M. Véron, P. Bastie, *Acta mater.* **45** (1997) 3277-3282.
[5] J. Kulda, P. Mikula, *J. Appl. Cryst.* **16** (1983) 498-504.
[6] P. Strunz, J. Šaroun, P. Mikula, P. Lukáš, F. Eichhorn, *J. Appl. Cryst.* **30** (1997) 844-848.
[7] http://omega.ujf.cas.cz/CFANR/k13.html
[8] http://omega.ujf.cas.cz/CFANR/access.html
[9] P. Strunz, R. Gilles, D. Mukherji, A. Wiedenmann, *J. Appl. Cryst.* **36** (2003) 854-859.

Computer Corner

Updates on Available Crystallographic and Powder Diffraction Software

(Suggestions, corrections, comments and articles on new or updated software are appreciated; especially if you know of new program features, program updates and announcements that should be mentioned here).

Lachlan M. D. Cranswick
Canadian Neutron Beam Centre (CNBC),
National Research Council (NRC),
Building 459, Station 18, Chalk River Laboratories,
Chalk River, Ontario, Canada, K0J 1J0
Tel: (613) 584-8811 ext 3719; Fax: (613) 584-4040
E-mail: Lachlan.Cranswick@nrc.gc.ca
WWW: http://neutron.nrc.gc.ca/

Rietveld Software Updates (as of 9th November 2007):

Hugo Rietveld website:	http://home.wxs.nl/~rietv025/
Armel Le Bail website:	http://sdpd.univ-lemans.fr/
BGMN (24th Sep 2007):	http://www.bgmn.de/
BRASS (20th Dec 2006)	http://www.brass.uni-bremen.de/
DBWS (22nd February 2000):	http://www.physics.gatech.edu/downloads/young/download_dbws.html
DDM (25th May 2006):	http://icct.krasn.ru/eng/content/persons/Sol_LA/ddm.html
Debvin (ftp download site not connecting):	http://users.uniud.it/bruckner/debvin.html
GSAS (24th Sep 2007):	http://www.ccp14.ac.uk/ccp/ccp14/ftp-mirror/gsas/public/gsas/
EXPGUI (30th April 2006):	http://www.ncnr.nist.gov/programs/crystallography/
Jana (1st October 2007):	http://www-xray.fzu.cz/jana/Jana2000/jana.html
LHPM-Rietica (19th July 2007):	http://www.rietica.org/
MAUD for Java (GPL'd) (9th Nov 2006):	http://www.ing.unitn.it/~maud/
MXD (27th July 2007):	http://www-cristallo.grenoble.cnrs.fr/Prog_Cristallo/
PowderCell (15th November 2006):	ftp://ftp.bam.de/Powder_Cell/

Prodd (19th August 2003): ……………… http://www.ccp14.ac.uk/ccp/web-mirrors/prodd/~jpw22/
Profil (24th May 2001): ……………… http://img.chem.ucl.ac.uk/www/cockcroft/profil.htm
Rietan 2000 (GPL'd) (15th March 2006)
http://homepage.mac.com/fujioizumi/rietan/angle_dispersive/angle_dispersive.html
Fullprof Suite (including Winplotr)
(October 2007): ……………… http://www.ill.fr/dif/Soft/fp/
XND (20th September 2007): ………….. ftp://ftp.grenoble.cnrs.fr/xnd/
XRS-82/DLS76: ……………… http://www.crystal.mat.ethz.ch/Software/index

Most of the above Rietveld programs are also available via the CCP14 website (http://www.ccp14.ac.uk/mirror/).

Summary lists of some software available via the EPSRC funded CCP14 website:

"What do you want to do?" (lists of software by single crystal and powder methods)
http://www.ccp14.ac.uk/mirror/want_to_do.html

Anharmonic Thermal Refinement Software: ……………… http://www.ccp14.ac.uk/solution/anharmonic/
Data Conversion for Powder Diffraction: ……………… http://www.ccp14.ac.uk/solution/powderdataconv/
Image Plate Software: ……………………………… http://www.ccp14.ac.uk/solution/image-plate/
Incommensurate Structure Software: ……………… http://www.ccp14.ac.uk/solution/incomm.htm
Indexing Software for Powders: ……………… http://www.ccp14.ac.uk/solution/indexing/
LeBail Method for Intensity Extraction: ……………… http://www.ccp14.ac.uk/solution/lebail/
Pawley Method for Intensity Extraction: ……………… http://www.ccp14.ac.uk/solution/pawley/
PDF, High Q Powder diffraction Analysis Software: http://www.ccp14.ac.uk/solution/high_q_pdf/
Peak Find/Profiling Software for Powder Diffraction: http://www.ccp14.ac.uk/solution/peakprofiling/
Pole Figure and Texture Analysis Software: ……………… http://www.ccp14.ac.uk/solution/pole_figure/
Powder Diffraction Data Visualisation: ……………… http://www.ccp14.ac.uk/solution/powder_data_visual/
Rietveld Software: ………………………………… http://www.ccp14.ac.uk/solution/rietveld_software/
Search-Match Phase Identification Software: …………… http://www.ccp14.ac.uk/solution/search-match.htm
Single Crystal Suites linking to multiple programs relevant to Chemical Crystallography:
http://www.ccp14.ac.uk/solution/xtalsuites/
Spacegroup and Symmetry operator determination software and source code:
http://www.ccp14.ac.uk/recomm/sym_operators_to_spacegroups.html
http://www.ccp14.ac.uk/recomm/spacegroups_to_sym_operators.html
Spacegroup and Structure Transformation Software: http://www.ccp14.ac.uk/solution/transform/
Structure Conversion and Transformation: ……………… http://www.ccp14.ac.uk/solution/structconv/
Structure Drawing and Visualisation: ……………… http://www.ccp14.ac.uk/solution/structuredrawing/
Unit Cell Refinement of Powder Diffraction Data: http://www.ccp14.ac.uk/solution/unitcellrefine/

How to receive the IUCr CPD Newsletter

If you wish to be added to the mailing list for the Newsletter of the IUCr Commission on Powder Diffraction or have changed address, please contact the Chairman:
Robert Dinnebier (r.dinnebier@fkf.mpg.de).

The Newsletter can also be downloaded in electronic format, as a pdf file, from the CPD web-site.

Companies

If you would like to advertise in this twice-yearly newsletter, please contact Robert Dinnebier
e-mail: r.dinnebier@fkf.mpg.de
Telephone: +49-711-689-1503
Fax: +49-711-689-1502

News from the
International Centre for Diffraction Data (ICDD)

12 Campus Boulevard
Newtown Square, PA 19073-3273, U.S.A.
Phone: +610.325.9814
Fax: +610.325.9823

www.icdd.com
www.dxcicdd.com
E-mail: info@icdd.com

Denver X-ray Conference

❐ **The 56th Annual Denver X-ray Conference** took place, 30 July through 3 August 2007 at the Sheraton Hotel in Colorado Springs, Colorado. Characterized by its traditional camaraderie, the conference experienced its highest attendance numbers in recent years. The nearly 550 attendees and exhibitors enjoyed the scientific exchange that transpired in the 16 workshops and 16 special sessions, held throughout the week. The conference also provided a forum for networking among scientists, both beginners to experts, working in the X-ray materials analysis fields.

Several awards were presented as well:

- ➸ Recognizing distinguished work in powder diffraction, the 2007 Barrett Award was presented to Sunil K. Sinha, of the University of California San Diego, La Jolla, CA. Sunil later presented a talk on: *What We Can Learn About the Structure and Dynamics of Surfaces and Thin Films from Off-Specular Scattering.*


Sunil Sinha (left) receives the Barrett Award from Cev Noyan (right).

- ➸ The 2007 Jenkins Award, which is awarded for lifetime achievement in the advancement of the use of X-rays for materials analysis, was presented to Ting C. Huang, Emeritus, IBM Almaden Research Center, San Jose, CA. The conference was honored to have Phyllis Jenkins present for this momentous occasion. Ting also received the 2007 Distinguished Fellow Award for his long and meritorious service to the ICDD.


Vic Buhrke (left) presents the Jenkins Award to Ting Huang (right), (Phyllis Jenkins, center).

- ➸ Tamás Ungár, of Eötvös University Budapest, Budapest, Hungary, became the recipient of the 2007 Hanawalt Award. This award honors scientists for important, recent contributions to the field of powder diffraction. Tamás was recognized for his work, *The Dislocation Model of Strain Anisotrophy.*

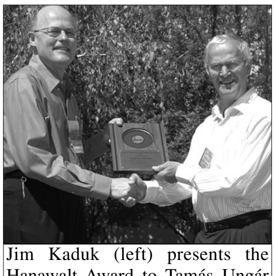
Jim Kaduk (left) presents the Hanawalt Award to Tamás Ungár (right).

At the conclusion of the conference, Dr. Vic Buhrke, Consultant, Portola Valley, CA, retired as Chairman of the DXC Organizing Committee. The Committee presented Vic with a plaque to acknowledge their appreciation for his years of dedication and service to the conference. Vic will remain a member of the Committee. Congratulations to our new Chairman, Dr. Bob Snyder, Georgia Institute of Technology, Atlanta, GA! The Committee is also pleased to welcome two new members to the Organizing Committee: Thomas Blanton of Eastman Kodak Company, Rochester, NY and Rene Van Grieken of the University of Antwerp, Antwerp, Belgium.


Newly-elected DXC Chairman, Bob Snyder (left), acknowledges Vic Buhrke's five years of service as Chairman (right).

Make your plans to attend next year's conference, 4–8 August 2008, being held at the Marriott Denver Tech Center Hotel. The International Conference on Residual Stress (ICRS-8) will meet jointly with the DXC. Stay informed: www.dxcicdd.com.

Educational Events

In pursuing its commitment to the education of scientists in the fields of X-ray analysis, the ICDD offers an extensive program of learning opportunities.

Specialized Workshops

In their second year, the new ICDD workshops on **Specimen Preparation for XRF** and **Rietveld Refinement & Indexing** once again received rave reviews by scientists who sought training in these areas.

A completely hands-on, intensive, lab-oriented workshop, **Specimen Preparation for XRF** took our participants through all steps of preparing a specimen from sample to analysis. Fusions, presses, mills and grinders were utilized by the participants to prepare specimens brought from their own labs, followed by analysis using the live WDS instrument. Faculty members, John Anzelmo, Anzelmo & Associates; Larry Arias, Bruker AXS; and Richard Bostwick, Spex SamplePrep LLC guided our participants along the way, giving them valuable tricks of the trade to take back to their labs.

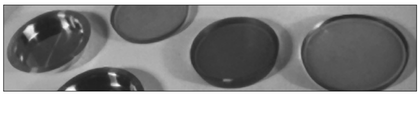

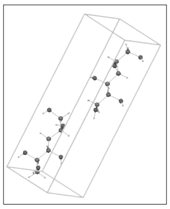

The **ICDD Advanced XRD Clinic** offers a small introductory section on the Rietveld Refinement method which always leaves our attendees wanting to know more on this technique. In response, the **Rietveld Refinement and Indexing Workshop** has been added to our repertoire of training opportunities. This fall, we hosted participants for an intensive three days of computer analysis using the Rietveld Method as a powerful tool for extracting accurate structural information from powder patterns of inorganic, organic, metal & alloy, macromolecular and coordination compounds. Participants were also guided by our expert faculty in performing quantitative phase analysis and obtaining microstructural information such as size strain and texture. The faculty included Drs. John Faber, Suri Kabekkodu, Fangling Needham, Joel Reid of the ICDD and James Kaduk of INEOS Technologies.

PPXRD-7

The Seventh Annual Pharmaceutical Powder Diffraction Symposium will take place in Orlando, Florida, 25–28 February 2008, with the optional workshop, Exercises in Quantitative Phase Identification, being held on February 25th. Stay informed: http://www.icdd.com/ppxrd/

Announcing … the updated ICDD Website!

The ICDD website is new and improved! Some of the new features include the easy navigation to Publications and Products, Clinics, Conferences, Grant-in-Aid, and Member News. To better serve our customers, you will also find multilingual versions of the website, currently available in Italian, Portuguese, French, Spanish, Russian, and Chinese.

The site also features some product tutorials focused on the embedded features in the **PDF-2** and **PDF-4+** databases. If you're a current user of these products, or are considering purchasing them, you may want to view these tutorials. They are designed to demonstrate the common features of the databases, hints and shortcuts, embedded application software in the PDF, use of embedded editorial and quality analyses, as well as the various features available in each database.

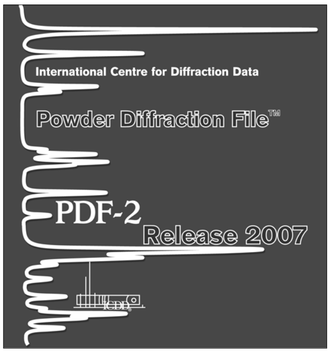

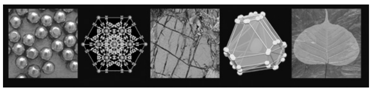

PDF-4/Organics 2008

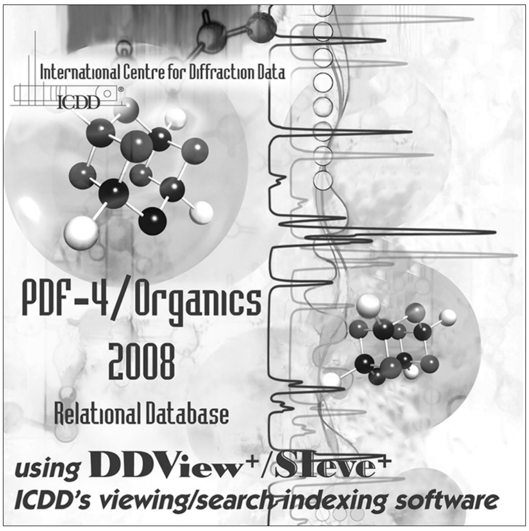

PDF-4/Organics 2008 is now available!

This latest edition of the organics file contains 341,540 new entries. Designed for rapid materials analysis, PDF-4/Organics 2008 excels in polymorph identification and formulation analysis. This database is a practical results-oriented product that combines drug active compounds with polymers (including starches and celluloses), excipients and pharmaceuticals. Our subfiles provide faster, efficient searches including Pharmaceuticals (3,577 entries), Bioactivity (9,010 entries), Excipients (1,623 entries) and Merck (1,574). New for 2008 is our statistical analysis package for x-y and histogram plots. The statistical package provides you with the power to examine the molecular symmetry, volume and packing of a compound to assist in polymorph identification. The database contains integrated viewing and searching software, **DDView+**, and as a value-added feature, a complimentary license for **SIeve+**, a search-index plug-in.

Further Information

To learn more about the ICDD, its products and services, please visit our web sites:

www.icdd.com and **www.dxcicdd.com**.